Ground-Coupled Air Waves:

A Seismological Case Study of the Explosion Quakes of the

2007 Eruption of Pavlof Volcano, Alaska

by

Cassandra M. Smith

A thesis submitted in partial fulfillment
of the requirements for the degree of
Master of Science
Department of Geology
College of Arts and Sciences
University of South Florida

Major Professor: Stephen McNutt, Ph.D.
Glenn Thompson, Ph.D.
Jochen Braunmiller, Ph.D.

Date of Approval:
February 26, 2015

Keywords: seismo-acoustic, Aleutian, gas release, infrasound

Copyright © 2015, Cassandra M. Smith

Acknowledgments

I would like to first and foremost thank my thesis advisor, Dr. Stephen R. McNutt, for his expert advice, guidance, and continual encouragement during my research and preparation for this thesis. I would also like to thank my committee members, Glenn Thompson, for his patience and never-ending help with coding, and Jochen Braunmiller, for his help with GMT as well as his continued support.

I could never have done this without all of the support of my family and friends. I would like to thank Heather McFarlin for always being willing to listen and Alex Farrell for the never ending candy pumpkin. I would like to thank Colin Maloney for his emotional support and for reminding me that mental health days are important. I am so grateful to my parents, Rodney and Glynis Smith, who have always encouraged me to follow my dreams, and supported me in all my choices. I would like to thank my siblings Elizabeth Bradley and William Smith for always being just a phone call away with support and reassurance.

Table of Contents

List of Tables

List of Figures

Abstract

An abnormally high number of explosion quakes were noted during the monitoring effort for the 2007 eruption of Pavlof Volcano on the Alaskan Peninsula. In this study we manually counted the explosion quakes from their characteristic ground-coupled air waves. This study makes an effort at better quantifying the number of explosion quakes and how the characteristic ground-coupled air waves are affected by wind direction and wind speed. Additionally this study investigates how the ground coupled air waves might be used in a monitoring or analysis effort by calculating energy release and gas mass release. Over 3.2×10^4 quakes were recorded. It was found that wind direction affects the travel time of the air wave by up to 0.7 seconds depending on station location and wind direction. Wind direction and speed, however, are demonstrated not to cause an appreciable difference in ground-coupled air wave frequencies or amplitude ratios. The energy release from the explosions is calculated to be 3.04×10^{11} J. and the total gas mass (assuming 100% water) released was 729 metric tons. These values are compared to other volcanoes in the literature and found to be somewhat lower. Nevertheless, the tracking of explosion quakes has the potential to become a valuable member of the seismic monitoring arsenal.

Chapter One:

Introduction

Pavlof Volcano is one of the most active volcanoes in the Aleutian Range, having erupted approximately forty times in recorded history. Historic eruptions from Pavlof have deposited measureable ash as far away as Sand Point (95 km). Ash erupted 26,000 years ago from the Emmons Lake Volcanic Complex has been found as far away as northwestern Canada (1600 km), showing that there is the potential for devastatingly large ash plumes from this complex.

The danger from eruptions containing ash is expansive. In the near field ash can be harmful to plants, animals, and human respiratory systems from both fallout and column collapse. In the case of Pavlof, since there is little infrastructure near the volcano, the far field effects of ash are more pressing. Ash can be caught in airplane turbines where it is reheated and melted, resulting in engine damage or shutdown and potential plane crashes. This occurred in 1989 when KLM Flight 867 flew through a day old ash cloud from Mt. Redoubt, resulting in temporary failure of all four engines.

It is important, from a monitoring standpoint, to know when there is the potential of an ash plume developing. Waythomas et al. (2006) determined the prevailing wind direction over the Cold Bay area to be predominately between northeast and southeast with the peak wind direction to be directly east for all altitudes up to 13 km. These wind directions would blow any plume towards Anchorage and through heavily traveled airspace. The Northern Pacific hosts the main flight paths that connect North America with East Asia (Neal et al., 2009). Approximately

10,000 passengers and 90 percent of Chinese imports fly over the Aleutians daily, with yearly flight counts at around 50,000 aircraft for these Trans-Pacific flights (Neal et al., 2004; AAWU, 2015; NOAA, 2008). The closest airport to Pavlof is located in Cold Bay (40 km west of the volcano) and has on average 20 flights per day, with the majority being local air taxi ventures.

There are several methods currently in use to monitor ash plume development. These methods heavily rely on visual inspection of the volcano, either through satellite imaging of the plume and/or SO_2 concentrations or by pilot reports. The problem with relying on visual based methods is that the weather in and around Pavlof and Cold Bay is commonly very cloudy and Pavlof is often obscured to line of sight or satellite visuals. The danger with relying on pilot reports is that at the speed planes travel by the time they see a plume they might already be too close for safety.

Therefore, it is desirable to develop a monitoring system that relies on a more weather hardy indicator such as seismic signals that may be usable in determining if an ash plume is developing. So far a reliable seismic relation to the development of an ash-laden plume has been elusive. Common seismic monitoring relies on looking for volcano-tectonic (VT) and long period (LP) earthquakes as indicators of building volcanic activity. Although, LP earthquakes are difficult to locate they are a common indicator of increasing volcanic activity. During the 2007 Pavlof eruption the Alaska Volcano Observatory (AVO) catalogue only shows a single 0.2 magnitude VT earthquake that occurred on September 12th (fig 1), after the peak of the eruptive activity, which occurred from August 30th to September 2nd. Another seismic monitoring method utilizes Real-time Seismic Amplitude Measurement (RSAM) plots which display the average seismic amplitude being recorded. For Pavlof, RSAM is more valuable than VT and LP tracking but still does not detail the entire explosive (and possibly ash plume forming) aspect of the

eruption.

It is the goal of this study to determine if there is a characteristic relation between explosion quake ground-coupled air waves, a seismic signal not commonly identified or catalogued by observatories, and the energy and mass of gas released by Pavlof during the 2007 eruption. Determining the amount of gas released by the volcano is the first step towards utilizing seismic signals in ash plume development monitoring. It is also necessary to determine if atmospheric conditions affect the recording of the explosion's ground-coupled air wave in order to determine conditions under which this type of data analysis may be detected and used reliably.

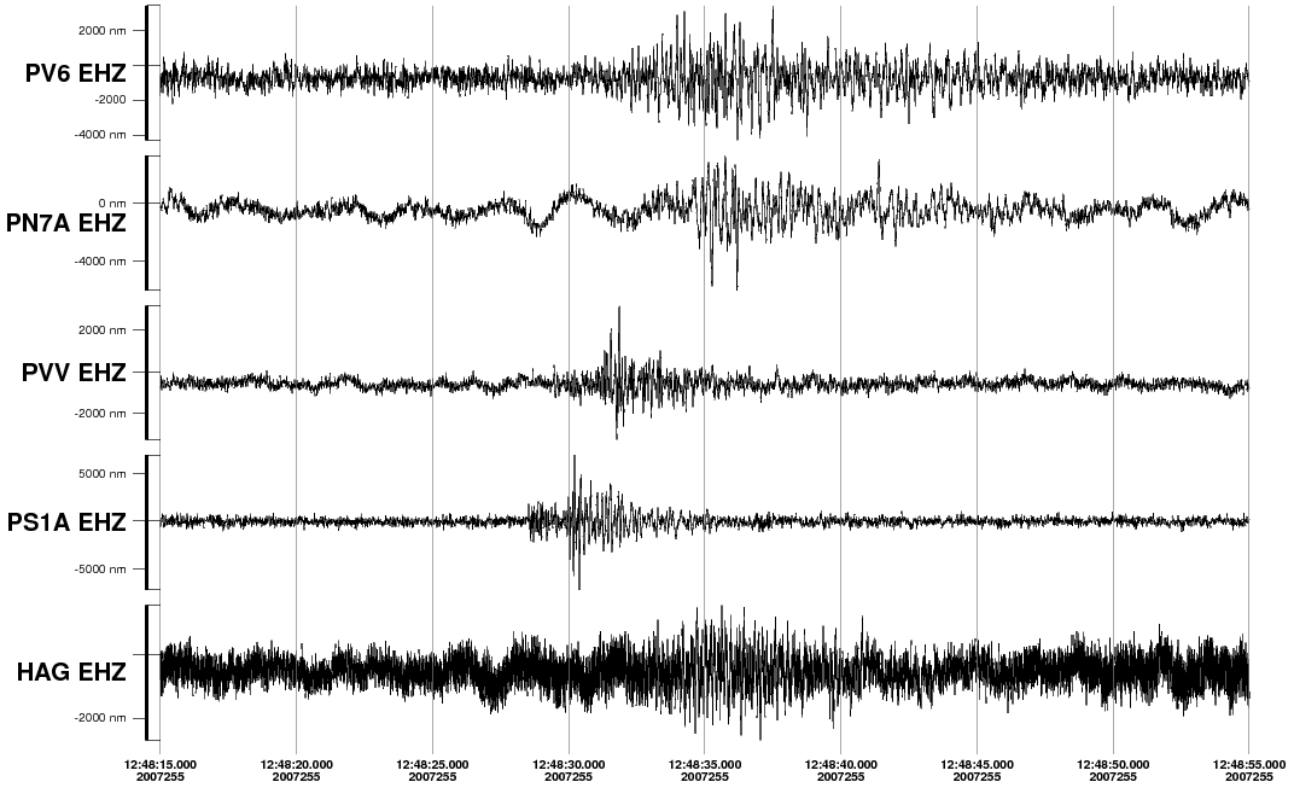

Figure 1: Single recorded earthquake in the AVO catalogue during the eruption. This earthquake was a 0.2 magnitude event. The visible P and S waves as well as a different arrival time pattern differentiate this earthquake from explosion quakes (seen in figure 4).

Chapter Two:

Literature Review

Geologic Setting

The Alaskan Peninsula-Aleutian Island arc is a volcanic arc created by the subduction of the Pacific plate beneath the North American plate. The Pacific plate is colliding with the North American plate resulting in the subduction of the Pacific plate. Minster and Jordan (1978) measured this collision to be occurring at a localized rate of 73 mm/yr. However, the more recent NUVEL-1 model looks at a more global scale and models the collision rate to be 53 mm/yr (DeMets et al., 1990). The resulting arc spans 2,500 km and consists of approximately fifty volcanoes that have been active in historical times with eighty additional volcanic centers that show evidence of being active over the past two million years (AVO, 2014).

Located at the western edge of the Alaskan Peninsula, Pavlof is a member of the Emmons Lake Volcanic Center – a caldera complex that contains six large volcanoes which trend northeast to southwest, including: Pavlof, Pavlof Sister, Little Pavlof, Double Crater, Mount Emmons, and Mount Hague, as well as many smaller vents and twelve cinder cones named alphabetically A-L (Kennedy and Waldron, 1955). This volcanic complex contains three nested calderas of Quaternary age. Volcanic ash that can be traced to the most recent of these caldera forming events was found 1600 km northeast of the complex in the Dawson area of the Yukon, dated to 26,000 years ago (Waythomas et al., 2006). Pavlof is located just outside the North Caldera scarp in the northeast corner of the complex (Waythomas et al., 2006). It has been

suggested that the entire volcanic complex is fed by a common mid-crustal (20km) magma unit (McNutt and Jacob, 1986).

Pavlof is located within the Shumagin seismic gap at 55°24.01'N, 161°54.63'W (fig 2) (McNutt and Jacob, 1986). It has a snow and ice covered peak with a maximum elevation of 2518 meters. Pavlof commonly erupts from the northern side of the volcano; however the vent location is mobile, and the 2007 eruption occurred on the south-east side of the mountain from a newly formed vent located approximately 200 m below the summit (fig 3). A typical eruption is Strombolian with a Volcanic Explosivity Index (VEI) of 2-3, including ash production, lava fountaining, spatter fed flows, and lahars. During the 1946 mapping of this region Kennedy and Waldron (1955) noted that glacial erosion had carved out sections of the volcanic edifice making the internal structure visible. This cross section showed lava flow layers alternated with beds of other volcaniclastic material in size from ash to bombs and blocks, pointing to a long and variable eruption history. Lahars and pyroclastic flows are common in Pavlof's eruptive history due to the summit snow and glacial ice that can be melted during an eruption.

The chemical compositions of the lavas produced from the volcanoes and cinder cones of the Emmons Lake Volcanic Center are andesite to basaltic andesite (52-63 wt % SiO_2) commonly containing between twenty and thirty percent phenocrysts of feldspar, olivine, hypersthene, and augite (Kennedy and Waldron, 1955; McNutt et al., 1991). The groundmass is microlitic feldspar, clinopyroxene, and brown glass (Kennedy and Waldron, 1955; McNutt et al., 1991).

Throughout recorded history ash fall has reached several nearby communities including Cold Bay (40 km west), King Cove (34 km southwest), Sand Point (95 km southeast), and Unga

Island (89 km east) (Waythomas et al, 2006; Kennedy and Waldron, 1955).

Eruptive History

Long term volcanic activity on the Alaskan Peninsula is evident from Tertiary aged tuffs, such as the Belkofski tuff, as well as intrusive quartz diorite stocks, basaltic necks, and andesitic sills that canvas the region (Kennedy and Waldron, 1955). Pavlof's edifice likely accumulated during the Quaternary, although a specific age is not established (Kennedy and Waldron, 1955). Pavlof's first recorded eruption in 1762 was noted by Grewingk (1850), however early eruption records are sparse and there is the possibility that some of them might refer to Pavlof Sister (Kennedy and Waldron, 1955). Since 1762, Pavlof has erupted approximately forty times roughly every 5-7 years (Waythomas et al., 2006; McGimsey et al. 2011). On average its eruptions have lasted for three months. Pavlof has few volcano-tectonic earthquakes, having instead, tremor, B-type events and explosion quakes making up the majority of its catalogue (McNutt and Beavan, 1981).

It has been shown that Pavlof's eruption patterns are susceptible to long period stress and strains resulting in a statistically significantly higher number of eruptions occurring during the fall months of September to November (McNutt and Beavan, 1981; McNutt, 1999). It is postulated by McNutt (1999) that lava is preferentially extruded during times that the volcano is underpinned by compressive stresses.

The two eruptions prior to 2007 occurred in 1986 and 1996, with a small event in 1990 that consisted mainly of traces of steam and visible melting of summit snow. The 1986 eruption sequence spanned from April to August and was VEI 3 at its maximum, with 5300 recorded explosion earthquakes (McNutt et al., 1991). In this eruption the explosions resulted in the

expulsion of volcanic bombs with small amounts of ash being produced (McNutt et al., 1991). The 1996 eruption of Pavlof started in September and ended in January 1997, reaching a maximum VEI of 2. This eruption was one of the first times where satellite imagery from the polar-orbiting AVHRR (Advanced Very High Resolution Radiometer) was used to monitor a volcanic eruption in near-real time (Roach et al., 2001). The use of the satellite data during this eruption brought to the forefront how poor weather conditions in this area do not always allow for visual verification of plume development, therefore highlighting the necessity for continued development of remote monitoring efforts.

The 2007 Eruption

Nearby communities to the Emmons Lake Volcanic Center include Cold Bay, King Cove, and Sand Point. These towns have small populations with robust fishing ventures; aviation is the main mode of transport in and out of these areas (Waythomas et al., 2006). Unlike most volcanoes - which show seismic activity increases in the days or weeks prior to an eruption - Pavlof commonly has rapid eruption onset with little to no seismic precursors. This lack of precursory warnings combined with the commonly bad weather and visibility in the Cold Bay area results in Pavlof's eruptions being of particular danger to the many aviation routes that traverse this airspace.

The seismic monitoring network on Pavlof was first established in 1973 by the Lamont-Doherty Earth Observatory (LDEO) and operated until 1990. A network was re-established by AVO in July 1996 (Roach et al., 2000). During the 2007 eruption there were five short period stations functioning within 12 km of the summit. There was one pressure sensor co-located with PN7A, however, it was only partially functioning during the eruption. The closest weather

station was station PACD, operated by NOAA and located at the Cold Bay Airport, 40 km to the west. Satellites are used to monitor for thermal anomalies and plume development. However, due to the commonly bad visibility in this area seismic data remains to be the closest and most reliable monitoring format available.

Eruption Timeline

The 2007 eruption took place after a repose period of almost 11 years – almost double the normal repose time of 6-7 years. Pavlof erupted on August 14, 2007, after less than one day of seismic ramp up. In contrast to previous, longer, eruptions this eruption only lasted for thirty days ending on September 13, 2007.

By the close of Aug 14th, 2007 AVO had raised the Aviation Color Code/Volcano Alert Level (ACC/VAL) to Yellow/Advisory due to the rapid increase in seismicity over the first day. However, there were no visible indications of eruption from either observers in Cold Bay or by satellite (McGimsey et al. 2011). Overnight the Advanced Very High Resolution Radiometer (AVHRR) recorded a thermal anomaly, which in conjunction with still increasing seismicity prompted AVO to raise the ACC/VAL to Orange on August 15, 2007 (McGimsey et al. 2011). Over the course of the eruption over 40 lahars were recorded traveling down the southern flank inundating an area measuring $2x10^6$ m^3 and entering the sea (Waythomas et al., 2008). A 565 m long, spatter fed, rootless lava flow also developed and was visible to individuals living in Sand Point as “orange streaks” and “glows” on the southern flank (Waythomas et al., 2008; McGimsey et al. 2011), and led to thermal anomalies detected by satellite remote sensing techniques. Tremor and repetitive explosion signals indicated that this was a continuous Strombolian style eruption (McGimsey et al. 2011). Although the main explosive peak of the

eruption was over by September 13th, and this is the AVO given end date of the eruption, the ACC/VAL was not decreased from Orange to Yellow until September 20th and not until October 5th was it reduced back to Green.

Previous Work on the 2007 Eruption

A previous investigation into the 2007 explosion quakes at Pavlof explored the utility of coda wave interferometry (Haney et al., 2009). Coda wave interferometry can be used to help discriminate between source and path effects. Haney et al. (2009) used the repetitive, emergent ground wave that occurs prior to the ground-coupled air wave of the explosions to investigate the potential of changing conduit dimensions. In this work only stations PN7A and PV6 were utilized and they were low pass filtered below 4 Hz. By determining a master event and cross correlation techniques they were able to identify 300-400 explosions per day from August 30th to September 11th. Changes in these quakes' characteristics were used to estimate changing conduit dimensions throughout the eruption (Haney et al., 2009).

Ground-Coupled Air Waves

During the 2007 eruption Strombolian explosions were noted on the seismic record and visualized in FLIR imagery. These explosions have a distinctive appearance on seismograms. They appear as a repetitive, emergent, low frequency ground wave appearing on all stations at approximately the same time followed by a higher frequency spike at times which increase with station to vent distance. The exact arrival time of the ground wave is difficult to determine due to its emergent nature. This time lag corresponds to the velocity of sound waves in air. This indicates that the spike is in fact an air wave that has its source at the vent. This pressure wave

presses down on the ground as it travels creating the seismic response (De Angelis et al., 2012; Sabatier et al., 1986). When this pressure wave is from an impulsive event the seismic station records the ground motion as an impulsive ground-coupled air wave spike. The pressure sensor co-located at PN7A corroborates the air-wave theory with impulses that show temporal alignment with the proposed ground-coupled air wave seismic pulse (fig 4). This type of seismo-acoustic signal has been studied at Stromboli (Braun and Ripepe, 1993; Ripepe, 1996; Ripepe et al., 2001), Karymsky (Johnson and Lees, 2000; Johnson et al., 1998), Sangay (Johnson and Lees, 2000), Arenal (Hagerty et al.' 2007), Mt. St. Helens (Johnson and Malone, 2007), Mt. Cleveland (De Angelis et al., 2012), Shishaldin (Petersen and McNutt, 2007; Vergniolle et al., 2004), and Pavlof (Garces and Hansen, 1998; Garces et al., 2000; Haney et al., 2009; McNutt, 1989; McNutt, 1999).

Source of the Air Wave

This air wave is an example of excess pressure – an instance where the pressure fluctuates either above or below the ambient atmospheric pressure (McNutt et al., 2015). In this study when we refer to the pressure we are talking about the excess pressure. The development of the air wave portion of these distinctive signals is one of debate. There exist two different ideas behind what is causing the impulsive seismic response: the vibrating bubble theory and the bursting bubble theory. However, there is also the possibility that these signals are the result of a combination of both of these sources, or that they both may be accurate in slightly differing circumstances (Garces, 1997).

Vibrating bubble theory

First there is the idea put forth by Vergniolle and Brandeis (1996) that an over-pressured bubble at the upper surface of the conduit vibrates before bursting. It is this vibration prior to bursting that is hypothesized to cause the recorded pressure waves. They propose that as a slug of gas rises through the conduit it becomes over-pressurized. At the magma-air interface the rising inertia of the bubble and its over-pressurization cause the bubble to expand past equilibrium and subsequently recompress. The model they propose has this cycle of vibration occurring once before the skin of magma becomes unstable and bursts. This vibration, rather than the bubble burst, produces the majority of the energy released (Vergniolle and Brandeis, 1994). This model was studied at Stromboli and Etna, both in quasi-permanent states of Strombolian eruption (Vergniolle and Brandeis, 1996; Vergniolle et al., 1996). Explosion quakes at Shishaldin had dominant frequencies of approximately 1 Hz, closely matching that which can be modeled by a vibrating bubble (Vergniolle et al., 2004).

Bursting bubble theory

The alternative theory behind the source cause of the ground coupled air wave is that when a Strombolian type gas bubble breaks at the vent-air interface that the explosion sends out a high frequency pulse which is recorded as a spike. The bursting of the bubble at the vent-air interface is analogous to a balloon breaking. The frequency of a balloon bursting is inversely proportional to its radius with high frequencies characteristic of small radii, e.g. 30 Hz for a 5 m. radius bubble (Vergniolle et al., 2004). In addition to this high frequency spike, the short duration of the impulsive event points to an explosive release, assumed by Johnson et al. (2003) to be the result of an impulsive thrust force, such as that from a bubble bursting at the vent. McNutt (1986) also categorizes these ground-coupled air waves as an ‘air-shock phase,’ the

result of an explosive ‘pop’. Braun and Ripepe (1993) used seismic gun experiments to determine that the sound pulse is ‘pushing’ on the ground as it travels. This ‘push’ is enhanced by the unconsolidated material that commonly covers volcanic regions, creating a favorable impedance contrast for high energy transmissions between the air waves and the ground (Braun and Ripepe, 1993). McNutt (1986) also utilized travel-time curves to determine that this air-shock phase was traveling at the speed of sound in the atmosphere, concluding that it was in fact an atmospheric rather than a ground wave. In studying the influence of gas release on seismic signals at Stromboli Volcano, Ripepe (1996) suggested that those seismic signals that have a low frequency component followed by a high frequency component with a simultaneously recorded air-pressure signal are the result of a single bubble of gas exploding at the vent-air interface.

Source of the Ground Wave

The emergent ground wave that appears before the ground-coupled air wave lacks clear P and S waves. It is, however, repetitive in nature, with each station showing the same phase characteristics for each event. Johnson et al. (2003) give two possible explanations for the existence of this type of seismic energy preceding the air wave. First, they determine that it might be related to the explosion source located at some depth within the conduit. A second idea is that it might be related to fluid motion or the cracking of rock prior to the explosion. Another theory is that the low frequency component is considered to be the portion of energy that is emitted into the ground at the time of bubble burst (Braun and Ripepe, 1993). The seismic energy that is perpetuated through the ground is attenuated by the unconsolidated cone of the volcano, resulting in the low frequency signature (Johnson et al., 1998). For our analysis we assume that the seismic and acoustic sources are co-located and the seismic wave develops from

the energy being partially partitioned into the ground (e.g. Petersen and McNutt, 2006; Hagerty et al., 2000).

Previous Work with Ground-Coupled Air Waves

The attraction to utilizing these ground-coupled air waves comes from their distinctive, and therefore easy to pick, appearance and their compatibility with infrasonic measurements. De Angelis et al. (2012) were able to locate large explosions from Mt. Cleveland Volcano using the Okmok seismic network, 120 km. away, by utilizing ground-coupled air waves. Additionally, since ground-coupled air waves travel through the atmosphere, which has a more simplistic velocity structure than the ground, they suffer less from path effects than the associated seismic phases (Petersen and McNutt, 2006). In certain conditions they can be detected over large distances due to tropospheric ducting (De Angelis et al., 2012). In cases where the stratified atmosphere amplifies the waves of strong explosions at long distance it has also been noted that near to the source a 'shadow-zone' can occur (Johnson and Malone, 2007). This was seen in the 1980 eruption of Mt. St Helens where ground-coupled air waves appear at distance but within the first few tens of kilometers they do not (Johnson and Malone, 2007). Within several kilometers of the volcano however, tropospheric ducting such as this is less likely to occur and it is reasonable to assume homogeneous atmospheric conditions. De Angelis et al. (2012) utilized a specialized short-term average / long-term average (sta/lta) detector applied to data from the Okmok network to detect the explosions from Mt. Cleveland. By configuring the sta/lta detector to account for the slower air wave travel time and check for the expected move out between stations as well as utilizing local and regional infrasonic networks they were able to detect 20 'hidden' explosions. The definition of a 'hidden' explosion is one that was not detected by

satellites or by other monitoring methods, potentially due to cloud cover (De Angelis et al., 2012). The De Angelis et al. (2012) code was tuned to work for those values that would result from a Mt. Cleveland explosion reaching the Okmok network. They state that with an eruption smaller than VEI 3, of which the Pavlof 2007 eruption was, the explosion signals generated are unlikely to be recorded outside of a local network within several kilometers of the vent (De Angelis et al., 2012).

Johnson and Lees (2000) looked at degassing events at Karymsky Volcano in Russia and Sangay Volcano in Ecuador. They recorded short and impulsive onsets of an air wave that were associated with temporal acoustic pressure sensor records. They associated these impulsive recordings with gas explosions located at the vent. One key observation made by Johnson and Lees (2000) was the considerable scatter in the ratio of seismo-acoustic energy as determined by plotting the normalized values of seismic amplitude (velocity) against the acoustic sensors amplitude (pressure). They list several reasons that might account for this scatter, including: (1) wind/weather, (2) depth of explosion source in conduit, (3) variable amounts of debris overlaying the conduit that might absorb the acoustic energy, and (4) preferential coupling of the energy into either the air or ground depending on the magma's impedance (Johnson and Lees, 2000).

When working with ground-coupled air waves it is necessary to account for atmospheric conditions that may affect how the air wave travels. This includes wind direction and temperature. The average daily temperature range at Pavlof over this time was only 4.4^{o}Celsius. Johnson et al. (2003) calculated that for the temperature fluctuations at Karymsky to influence the air wave travel time that they would need to have a range of 24^{o} Celsius. In their investigations they found this range to be implausible, and therefore they focused, as we will, on

wind direction. Johnson et al. (2003) determined that wind direction could alter the apparent acoustic velocity of the wave, and utilized a 0.5 s. range on their origin times to account for this. We will investigate further to determine a more exact range depending on station locations and wind directions.

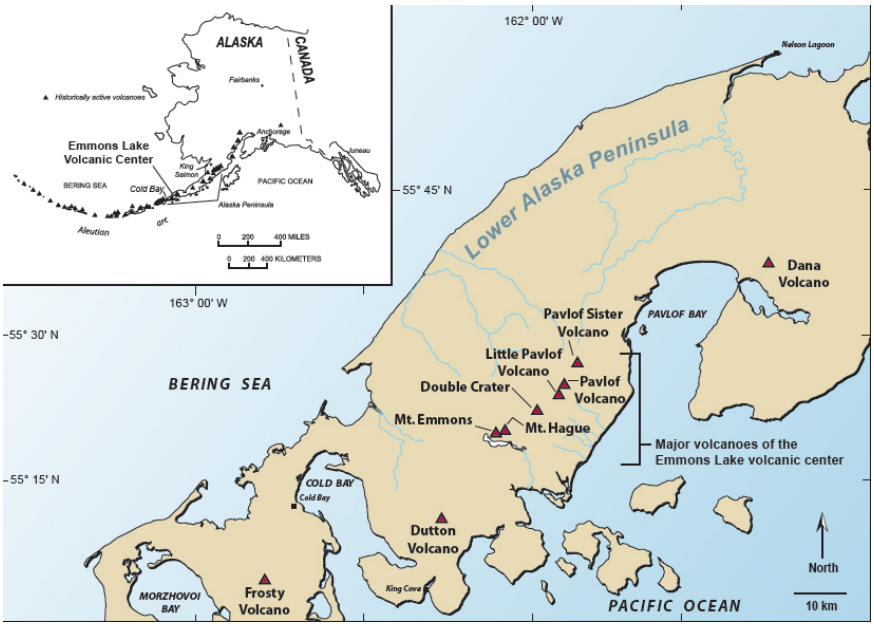

Figure 2: Location map of Emmons Lake Volcanic Center. Located at the end of the Alaskan Peninsula, Pavlof is a stratovolcano in the Emmons Lake Volcanic Center. Image from Waythomas, Alaska Volcano Observatory/U.S. Geological Survey.

Figure 3: Location of the 2007 crater. Located on the southeast face of the volcano, the crater is approximately 50 m wide and located 200 m from the summit. Image edited from Waythomas, Alaska Volcano Observatory/U.S. Geological Survey.

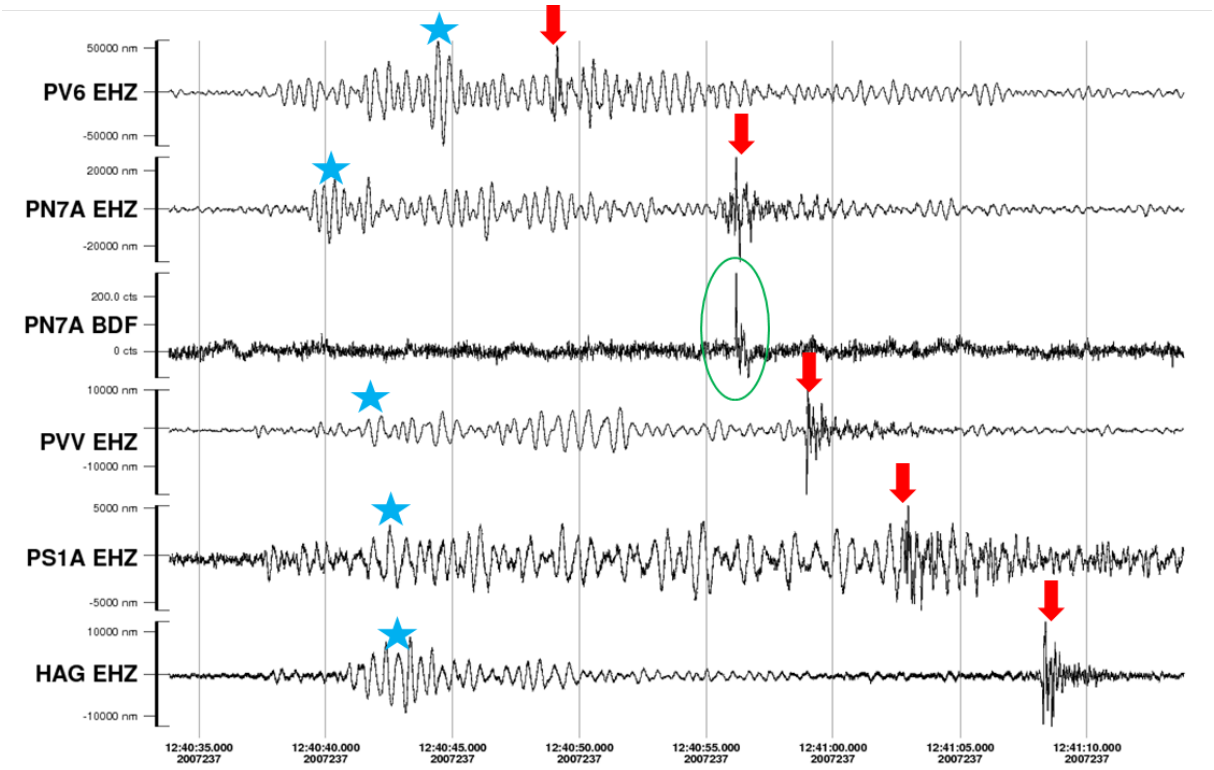

Figure 4: Example of ground-coupled air waves. The red arrows point to the high frequency, impulsive ground-coupled air waves. The blue stars are located over the repetitive, emergent, ground phase used in our measurements. The green oval is on the pressure sensor co-located with PN7A and shows the temporally aligned pressure pulse with the ground-coupled air wave on PN7A. The stations are ordered from the top down with increasing distance from the volcano.

Chapter Three:

Procedures and Methodology

AVO digitally recorded telemetered seismic traces from five stations surrounding Pavlof during the 2007 eruption sequence (fig 5). PN7A, PS1A, PVV, and HAG are one component, short-period, Mark L-4 1 Hz seismometers with a 100 sample per second rate. PV6 is a 3 component, short-period 2 Hz, L22D seismometer also with a sample rate of 100 samples per second (table 1). All five seismometers were actively recording throughout the 2007 eruption, except for a few periods of signal drop out which occurred most notably on September 7th across three stations - HAG, PVV, PS1A - for approximately 10.5 total hours per station. PS1A malfunctioned for the first 9 days of the eruption and PN7A malfunctioned for 22 hours on August 19th (Appendix A). The pressure sensor co-located at PN7A had noise issues for the majority of the eruptive period, however; there are several times that the pressure sensor did reliably record the pressure changes associated with the explosion quakes.

Haney et al. (2009) previously used cross correlations of the repetitive, emergent, ground wave at the northwest stations, on the radial component of PV6 and the vertical component of PN7A to tabulate the number of explosions per day. For this study we choose to look instead at the ground-coupled air wave as it appeared across all five functioning stations. This allowed us to identify a higher number of total quakes that (1) did not appear as clearly on the northwesterly stations and (2) that occurred during times of high activity and/or wind noise where the repetitive ground waves were obscured yet the air wave spikes were still visible. The vertical components

of these seismograms were manually inspected in 40 second intervals for explosion quakes. No frequency filter was initially utilized. Explosion quakes were identified by the discrete air wave and higher frequency as well as the separation in arrival times of the air wave between stations which follow the speed of sound in air (fig 6). Once identified the clearest signal time was manually recorded to the nearest second along with the station name. The arrival times were corrected for air travel time to determine origin times. These corrections were different for each station in reference to the distances from the 2007 vent to each station utilizing the speed of sound waves in air of 320m/s. For our calculations we utilized the assumption that the explosions originated at the interface of the conduit and atmosphere at the vent opening. The 2007 vent was located on the southeast side of the volcanic edifice, farther down the flank from previous eruptions. We plotted the explosion quake data to show rate per day, hour, and minute (fig 7). From the collected signal times we wrote a MATLAB code utilizing the Waveform Toolbox (Reyes and West, 2011) that gathered and recorded each station's amplitude for each explosion. This code and a more detailed description of its process can be found in Appendix B.

By mining the AVO eruption response logs we were able to gather ash and plume data from the variety of sources reporting to AVO at that time, including: pilot reports (PIREPS), significant meteorological reports (SIGMETS) from NOAA, AVHRR (Advanced Very High Resolution Radiometer) satellite images, ASTER (Advanced Spaceborne Thermal Emission and Reflection Radiometer) images, photographs, webcam images, and visual reports from community members near Pavlof. These data were then plotted using different symbols according to reporting style (fig 8).

Wind

In addition to the seismic and plume data we looked up historical weather catalogues for Cold Bay in order to determine the atmospheric setting of the eruption. This data was gathered from the 1-minute ASOS (Automated Surface Observing System) data through the National Oceanic and Atmospheric Administration (NOAA).

In order to determine how wind affects the recording of explosion quakes we looked at travel times, frequencies, and amplitude ratios in relation to wind direction. We took the wind directions from the ASOS data and divided them into 45 degree bins with the eight main compass directions at the centers of each bin. When plotting out the wind directions (fig 9) it became clear that the four main wind directions during this time period were from the southeast, west, north, and northwest. Since the times registering north and northwest were mainly prominent over the same period and fluctuated rapidly between the two we choose to group them together into a north/northwest designation for these analysis.

Taking a sample of explosion quakes from times during each of these primary wind directions we measured travel time differences. We first manually measured the time between the explosion quake spike and a prominent repetitive ground phase (fig 4). The ground wave that appears before the explosion quake spike is emergent and therefore has no clear P or S wave. However, since the ground waves are repetitive it is possible to use one of these repetitive phases for these measurements. In order to see if wind velocity was a factor we needed to reference the air wave travel times to the origin time rather than to the arbitrary, yet clear ground wave phase. However, since the origin time cannot be precisely determined from P or S waves we must calculate an inferred origin time to work with. To do this we first choose a reference event (September 2nd at 14:07:40) which occurred during a time of SSW wind direction and the wind

speed was at 1 knot. This direction combined with the low wind speed allows us to assume that the station recorded air waves in this event were not affected by either wind direction or speed. Using station HAG where the air wave was clearest we back calculated what the origin time of the event would have been by using the speed of sound in air and the distance from the vent to station HAG. We then took the difference between this origin time and the prominent ground phases on each station and used this as a correction factor for the air wave travel times. We grouped these travel times according to wind direction and took an average for each station and each wind direction. Theoretically the differences in wind direction and velocity should result in faster arrivals when the wind is blowing towards the station and slower arrivals when the wind is blowing away from the station and towards the vent. We calculated theoretical travel time values for each station by using the average wind speeds and directions. By comparing the measured and theoretical, calculated values we are able to determine if the wind direction and speed have an effect on the travel time of the air wave (fig 10).

In order to determine if the wind had an effect on the frequency of the ground-coupled air wave we plotted the frequency spectrum of the ground-coupled air wave. By taking a 5 second window - 2 seconds before and 3 seconds after - around the main amplitude spike, we guaranteed that the entire wave was captured by the spectra. The main frequency peak was then recorded and plotted into 1 Hz bins to determine if wind direction forced any trends in frequency content (fig 11). Examples of these spectra can be found in Appendix F.

Garces et al. (2000) hypothesize that the ratio between ground-coupled air wave amplitude and ground wave amplitude has the potential to be used to monitor magmatic gas content. To examine this for our dataset we plotted the amplitude ratios: color coded to wind direction, and size coded to wind speed in order to see if there was any trend. The same

prominent, repetitive, ground phase was used for the ground wave amplitude as was used in the travel time difference measurements. Linear regressions were plotted for each wind direction group and for the set of ratios as a whole (fig 12).

Gas

The ground-coupled air waves recorded at Pavlof show a higher average frequency than those recorded at Shishaldin, suggesting that they might result from bursting bubbles rather than vibrating bubbles (Vergniolle et al., 2004). For this investigation we assume bubble burst rather than bubble vibration as the air wave source. In order to calculate the energy or gas mass being released by these explosions we must first know the pressure fluctuation resulting from the bubble burst that created the ground-coupled air wave. Garces et al.'s (2000) looked at a similar problem where they determined the vertical ground velocity resulting from a pressure wave of given characteristics. Following is Garces et al.'s (2000) original equation for a sound wave incident to the ground at the grazing angle:

$$v_{lz} = \frac{p_o}{\rho}\left\{-\alpha_1 W_L e^{-j\alpha_{1z}} + \xi W_T e^{-j\beta_{1z}}\right\} \exp j(\xi x - \omega t) \qquad (1)$$

where: v_{lz} is the vertical particle velocity (m/s) recorded on the seismometer, p_o is the pressure (Pa) needed to create the recorded velocity response, ρ is the density (kg/m^3), α_1 is the vertical acoustic wavenumber (1/m), β_1 is vertical wavenumber (1/m), ξ is horizontal wavenumber (1/m), x is the wavelength (m), t is the period (s), ω is the angular frequency (1/s), W_T is the transverse transmission coefficient, and W_L is the longitudinal transmission coefficient (Table 2). The equations for W_L and W_T can be found in Appendix C and are from Brekovskikh (1980). Since we have the ground velocity from the seismometer amplitude we will use this equation to solve for the needed pressure (p_o) to create this velocity.

The ground-coupled air waves recorded show retrograde elliptical motion (fig 13) indicating that they are Rayleigh waves. Although Garces et al (2000) states that these equations are only viable for body waves we justify the use of the equation on the following assumption: since the ground surface located at the seismic sensor is not an idealized flat plane it is likely that the wave intersecting the ground surface is being transferred into the ground as both a P and an S_v wave. The Rayleigh wave-like motion can be accounted for as an interference of these two wave motions.

Once we have the pressure at the seismic station we can extrapolate back to what it would have been at the source rupture using the $^1/_r$ pressure decay law. We use the radius of the gas bubble as the source radius. In order to determine this radius we take the average frequency of the ground-coupled air waves at station PN7A and use ¼ wavelength. One quarter of the period is the initial rise time of the explosion, causing the initial pressure fluctuation. This rise time can be related to the wavelength where ¼ wavelength would be equivalent to the bubble's radius immediately prior to bursting (11 m). From the calculated source pressure and initial bubble volume we are able to calculate the kinetic energy released from explosions during the eruption:

$$PV = E \tag{2}$$

where P is the source pressure (Pa), V is bubble volume (m^3), and E is kinetic energy (J). The total mass of gas released is calculated by using the ideal gas law:

$$n = \frac{PV}{RT} \tag{3}$$

where n is the number of moles of gas released, P is the source pressure (Pa), V is bubble volume (m^3), R is the gas constant ($8.3145 \frac{J}{mole\ K}$) and T is temperature (K). The temperature used was 630^o Celsius, determined from FLIR images taken on August 18th (Read, 2007). After we have calculated the number of moles of gas we have to make an assumption on gas

percentages. The plume for the 2007 eruption of Pavlof was recorded as being mainly composed of steam and small amounts of ash (Waythomas et al., 2008). Therefore we can assume that all the gas released was water. From the number of moles of water we can calculate the total mass of water exsolved by the volcano. By calculating the energy/gas mass of each explosion event we can look at the cumulative release history of the eruption.

A Python code, given in Appendix D, was written and used for these calculations. The results of this code are highly sensitive to the set of variables values chosen for the Garces et al. (2000) equation. We have worked to make our assumptions reasonable.

The angles for θ and θ_1 were geometrically calculated using the distance and elevation differences from the summit to station. For the density of air (1 kg/m^3), the ground density (2700 kg/m^3), the speed of a sound in air (320 m/s), the P wave velocity in shallow, unconsolidated ground tephras (1500 m/s), and the S wave velocity in shallow, unconsolidated ground tephras (380 m/s), we use the same values for volcanic areas used by Garces et al. (2000) in their original paper. The velocity values for the P and S waves in the unconsolidated ground tephras are an estimation. The velocity of these waves in unconsolidated material at the ground surface is highly variable and changes both laterally and with depth. The values used here were determined by Garces et al. (2000) in his original use of this equation and due to lack of better measurements we have chosen to use them as well.

We used the amplitude values for station PN7A for these calculations. PN7A was co-located with the pressure sensor. Although the pressure sensor suffered from noise and mechanical issues for the majority of the eruption there were several instances where the explosion quakes ground-coupled air wave appeared on the pressure sensor as well. These instances allowed us to compare the pressure output from equation (1) with the direct pressure

measurement from the sensor. The calibration of the pressure sensor is 35 counts per Pascal (G. Tytgat, personal communication). The calculated pressures from equation (1) did not match with the pressures recorded by the pressure sensor. In order to bring the calculated pressures in line with the pressure recorded by the sensor we calculated an average multiplicative coefficient that when applied to the calculated measurements from equation (1) resulted in a close match to those pressures recorded directly by the pressure sensor (Table 3). This coefficient was 5.5.

The average frequency of the ground-coupled air wave was chosen to be 7 Hz. This value was determined by looking at the plots for the main frequency component of the ground-coupled air wave. The main frequency for station PN7A was 7 Hz, independent of the wind direction. We decided to use only a single frequency to maintain the speed and simplicity of the code. In order to change the frequency for each calculation the code would have to actively perform the Fourier transform for each of the 3.2×10^4 events and pick the peak, greatly increasing the computational power and time needed to run the code. The frequency is consistent with previously measured frequencies of explosions at Stromboli of 3-8 Hz (Ripepe et al., 1996).

This frequency is used to calculate the radius of the bubble at the source. Using a single frequency is further justified by an argument put forth by Vergniolle et al. (2004). Using laboratory experiments they determined that bubbles in well-developed slug flow – such as that seen in Strombolian activity like that present in the Pavlof 2007 event – are approximately constant in size, and occupying a large proportion of the main conduit (Vergniolle et al., 2004). For our calculation of the radius we directly use the frequency, so it would be a logical assumption to use the same frequency in order to maintain the bubble radius.

There are no direct measurements of the width of the conduit at the vent-air interface. However, using FLIR images of the lava extrusion and photographs of the crater after the

eruption, it is possible to determine the crater size and then extrapolate back to determine if our bubble radius is reasonable. Using a frequency of 7 Hz we get a bubble radius of ~11 m. This gives a bubble diameter of 22 m and following Vergniolle et al.'s (2004) conclusion that the bubble takes up a majority of the conduit, this would require a conduit diameter of approximately 25 m to allow for the bubble and surrounding magma skin. By examining the FLIR images and photographs of the crater we can determine that the summit crater is approximately 50 m in diameter (fig 14). Since the crater is likely some variation on a conical shape the vent-air interface that marks the top of the conduit would have to be smaller than 50 m. Therefore, a conduit diameter of 25 m. and a bubble radius of 11 m. is logical.

The volume of the exploding bubble is also directly calculated from this radius. There is no evidence of fire-fountaining, which would be manifested in codas of longer duration, and therefore no reason to assume the elongated gas slugs related to gas jetting. Since the explosion quakes recorded on the seismometers are of short duration we have assumed a spherical bubble model with an impulsive energy release (Johnson et al., 2003).

Sources of Error

The equations used to calculate energy and mass of gas released by the explosions are influenced by a few key variables. When writing this code we worked to make the most reasonable estimation of these variables and whenever possible utilized measured values. Two variable choices had the potential to greatly affect these calculations. The first is the chosen frequency. We chose to not calculate and pick the peak frequency for each event and instead use an average peak frequency. This frequency is utilized to calculate six of the variables in equation 1 including: the vertical acoustic wavenumber, the horizontal acoustic wavenumber, the vertical

wavenumber, the wavelength, the period, and the angular frequency. Additionally, the frequency was used to calculate the volume of the bubble used in the mass of gas calculation. In order to test how much of an effect this chosen frequency had on the results we ran the code with a range of frequencies from 1 Hz to 15 Hz and examined the trends. Both the mean energy and the mean water content per explosion show a decrease with increasing frequency with a range of approximately 2.5 orders of magnitude. This pattern and range is also seen with the total cumulative energy and total cumulative water content for the variation in frequency.

The second variable that has a large uncertainty is the temperature of the magma at the vent-air interface. The value used for this study was the highest recorded value by a FLIR camera during a helicopter flyover. Although this value (630 ^{o}C) is a very low estimate, as it is the only actual measurement made it is the one we chose to use. In order to test how much of an effect this chosen temperature had on the results we ran the code with a range of temperatures from 500 ^{o}C to 1500 ^{o}C in 100 ^{o}C increments and examined the trends. Since the temperature is not a factor in the energy calculation the energy values remained the same for the total range of tried temperatures. The water content per explosion shows a slight decrease with increasing temperature. This same trend is better illustrated in the total cumulative water released by the eruption, as temperature increases the total water released decreases covering a range of half an order of magnitude. Plots showing all of the relationships stated above can be found in Appendix F.

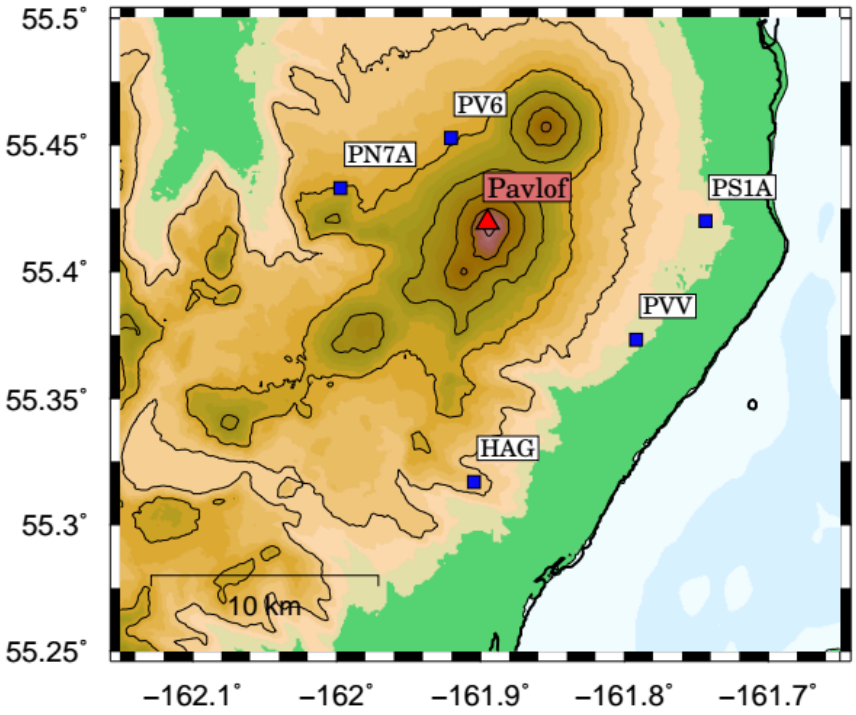

Figure 5: Station location map. The summit of Pavlof is represented by the red triangle. The seismic stations are blue squares.

Table 1: Seismic and Pressure Station Specifications

Station	Latitude	Longitude	Elevation (km above sea level)	Channel	Type	Sample Rate (Hz)	Distance to Vent (km)
HAG	55.3170	-161.9045	0.5160	EHZ	Mark L-4 1 Hz	100	11.2
PVV	55.3732	-161.7919	0.1730	EHZ	Mark L-4 1 Hz	100	8.40
PS1A	55.4201	-161.7437	0.2830	EHZ	Mark L-4 1 Hz	100	9.30
PV6	55.4528	-161.9205	0.7470	EHZ	L22D 2 Hz	100	4.40
PN7A	55.4329	-161.9973	0.8380	EHZ	Mark L-4 1 Hz	100	7.06
PN7A	55.4329	-161.9973	0.8380	BDF	Pressure	100	7.06

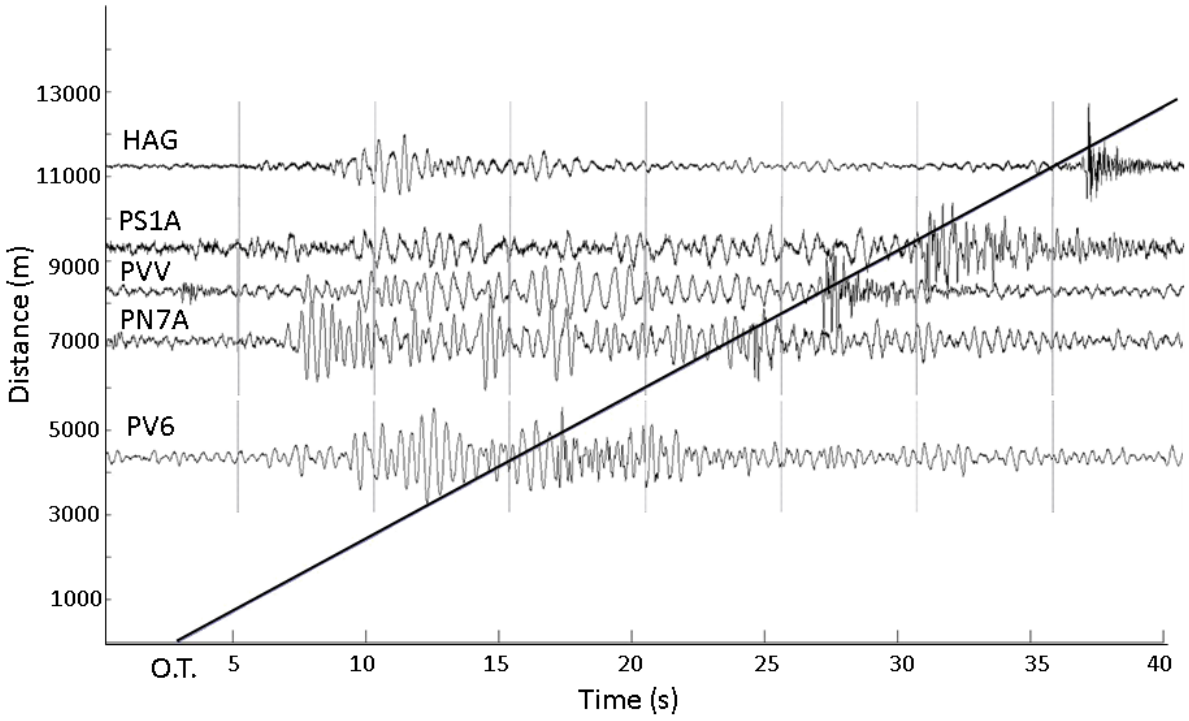

Figure 6: Distance-time plot of the ground-coupled air waves. The slope of the line is 320 m/s, showing that the wave causing this phase was traveling at the speed of sound in air. O.T. is the origin time of the blast.

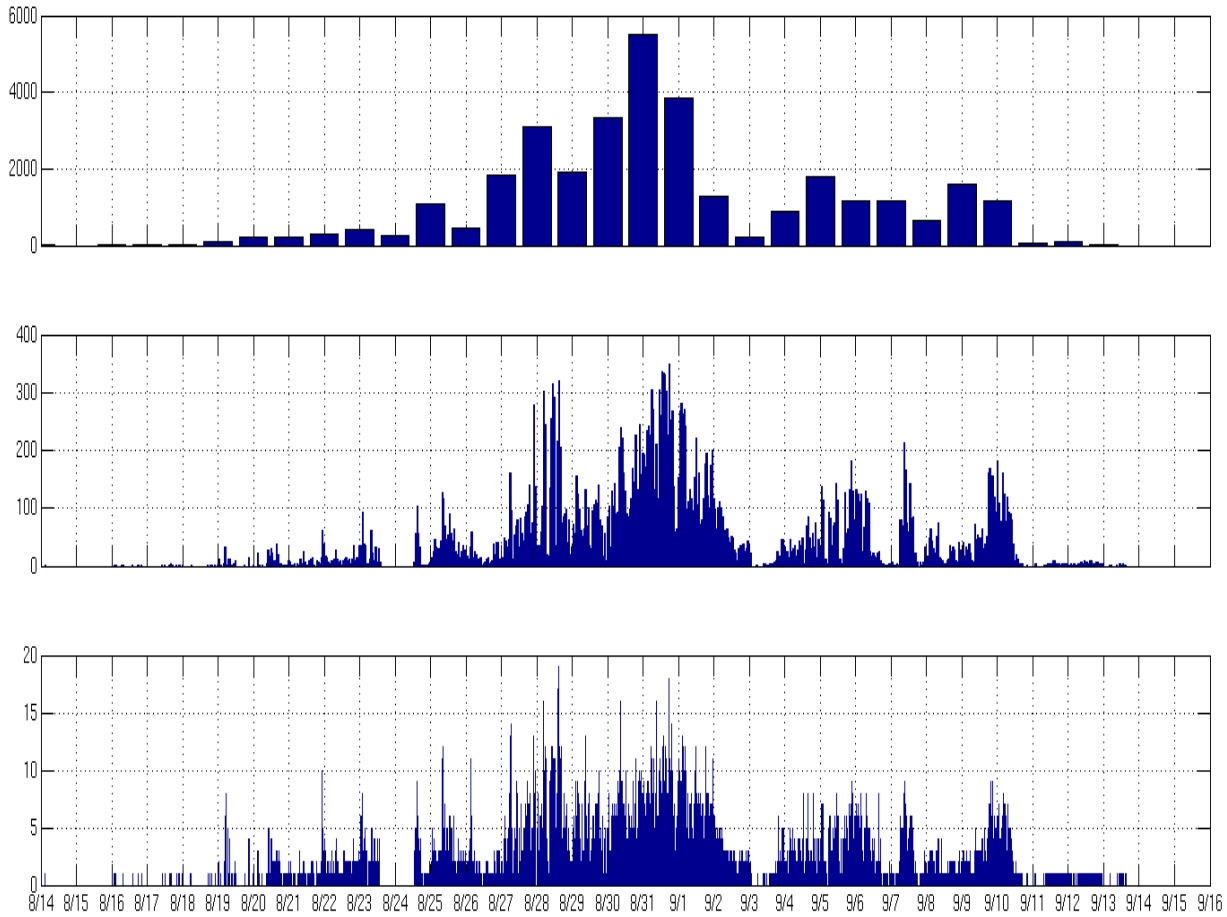

Figure 7: Explosion quake rate plots. The top plot is number of explosion quakes per day, maximum at 5500 on 8/31. The center plot is the number of explosion quakes per hour maximum at 350, and the bottom plot is the number of explosion quakes per minute, with a maximum at 19.

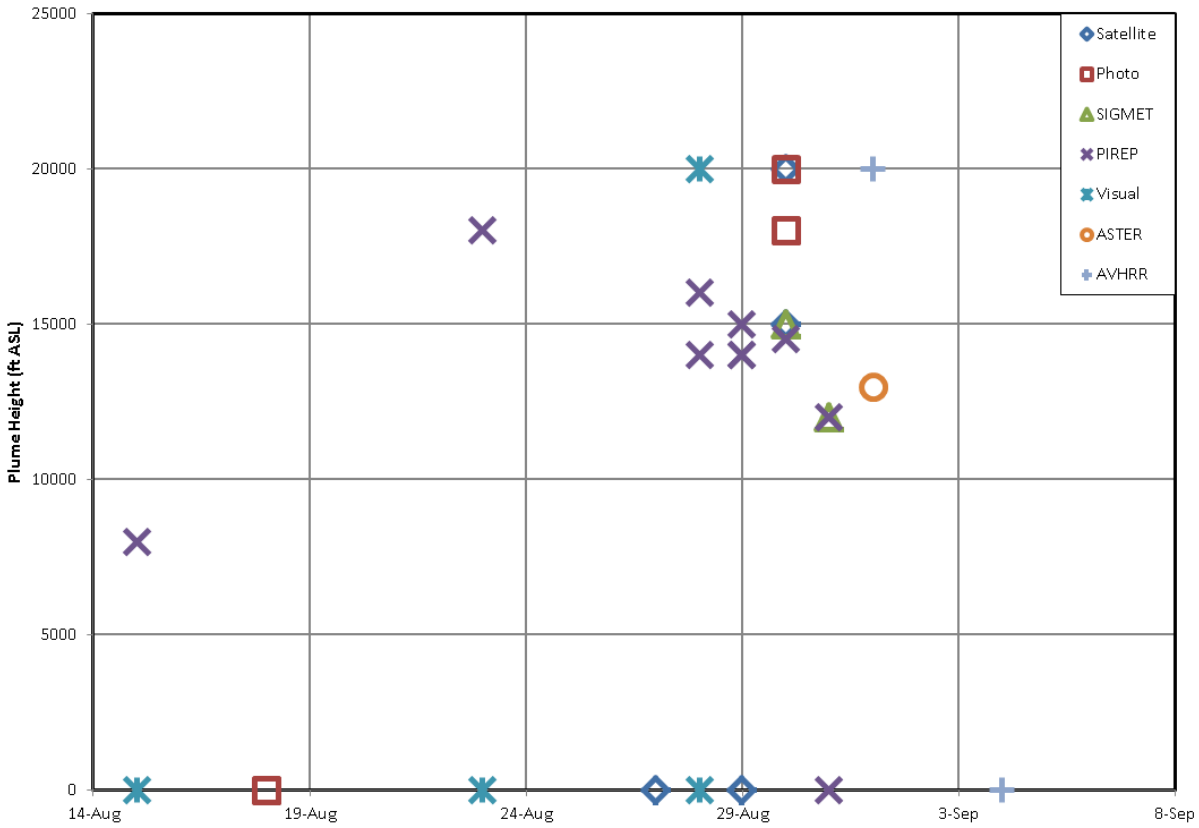

Figure 8: Ash/ plume reports. Different symbols correspond to the different reporting methods. Points that have an altitude of 0 are qualitative reports that noted that a plume was present but did not provide an estimate of height.

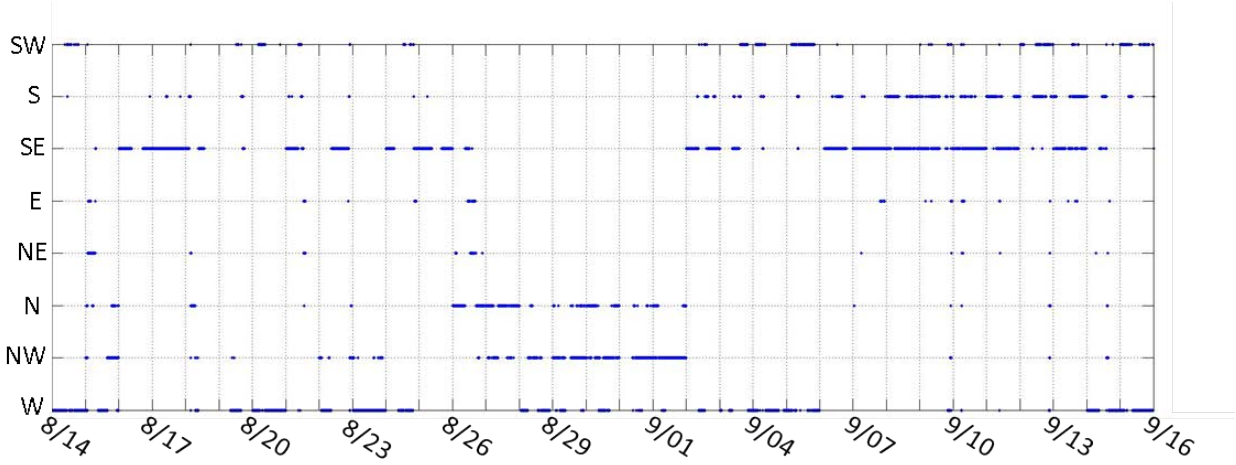

Figure 9: Wind direction each minute. Taken from NOAA ASOS data from Cold Bay and binned into 45 degree units corresponding to the eight main compass directions. This plot shows the patterns of what direction the wind was coming from. The wind data is recorded in one minute intervals.

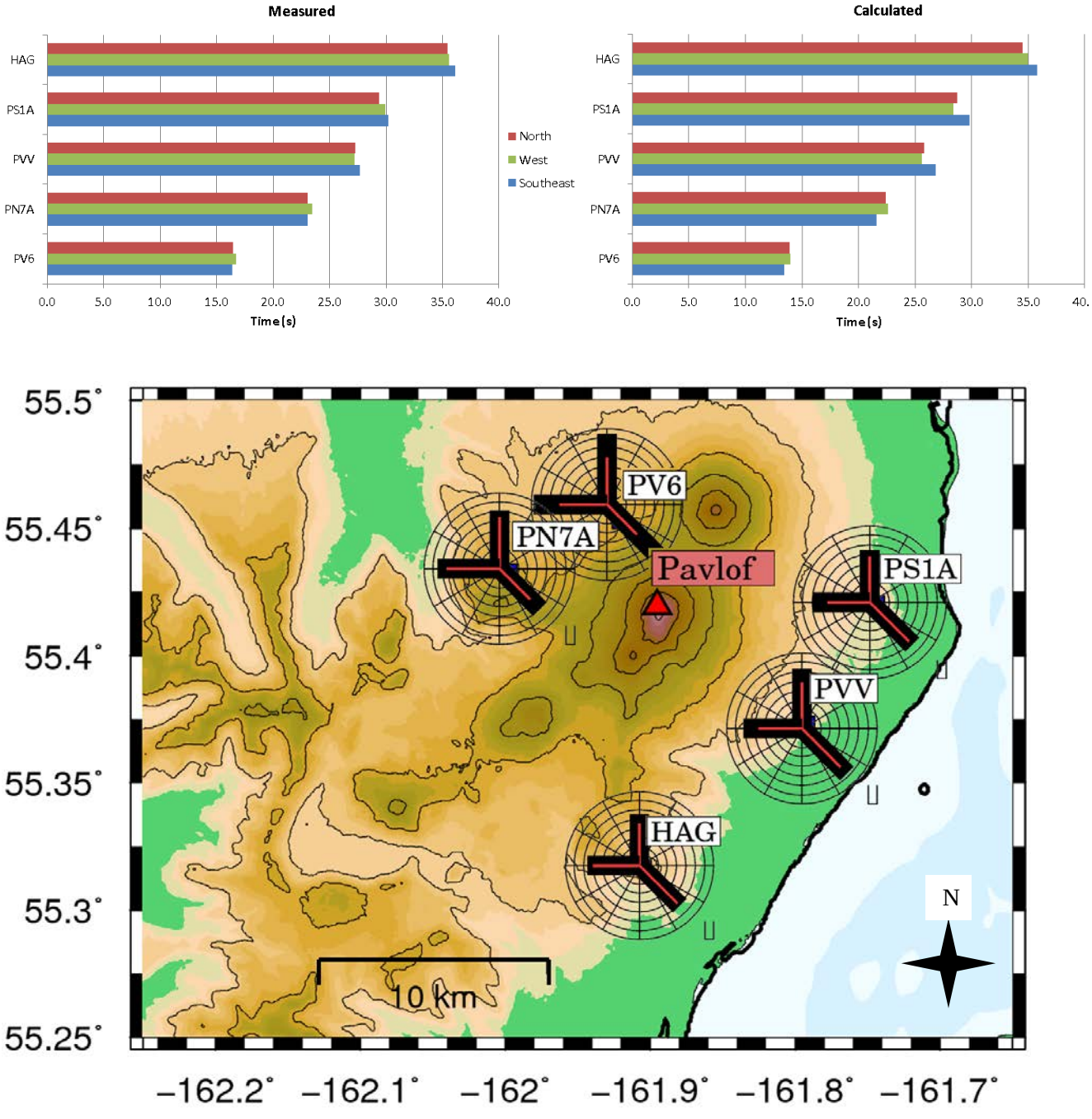

Figure 10: Average time between prominent ground phase and air wave. The top left plot shows the measured average time between the assumed origin time and the ground-coupled air wave. The travel-time differences between wind directions at different stations range from 0.4 to 0.7 seconds. The top right plot shows the calculated travel-times between the vent and station, using the average wind speed and direction for the selected times. The bottom frame shows these values plotted per station on a rose diagram. The thick black line shows the measured value, the thin red line shows the calculated value. The difference in lengths of the red and black lines shows the difference between calculated and measured values. Rose diagram circles are 1 second increments. For better visualization of the small scale differences the data is zoomed in to show only the last few seconds where the time difference occurs.

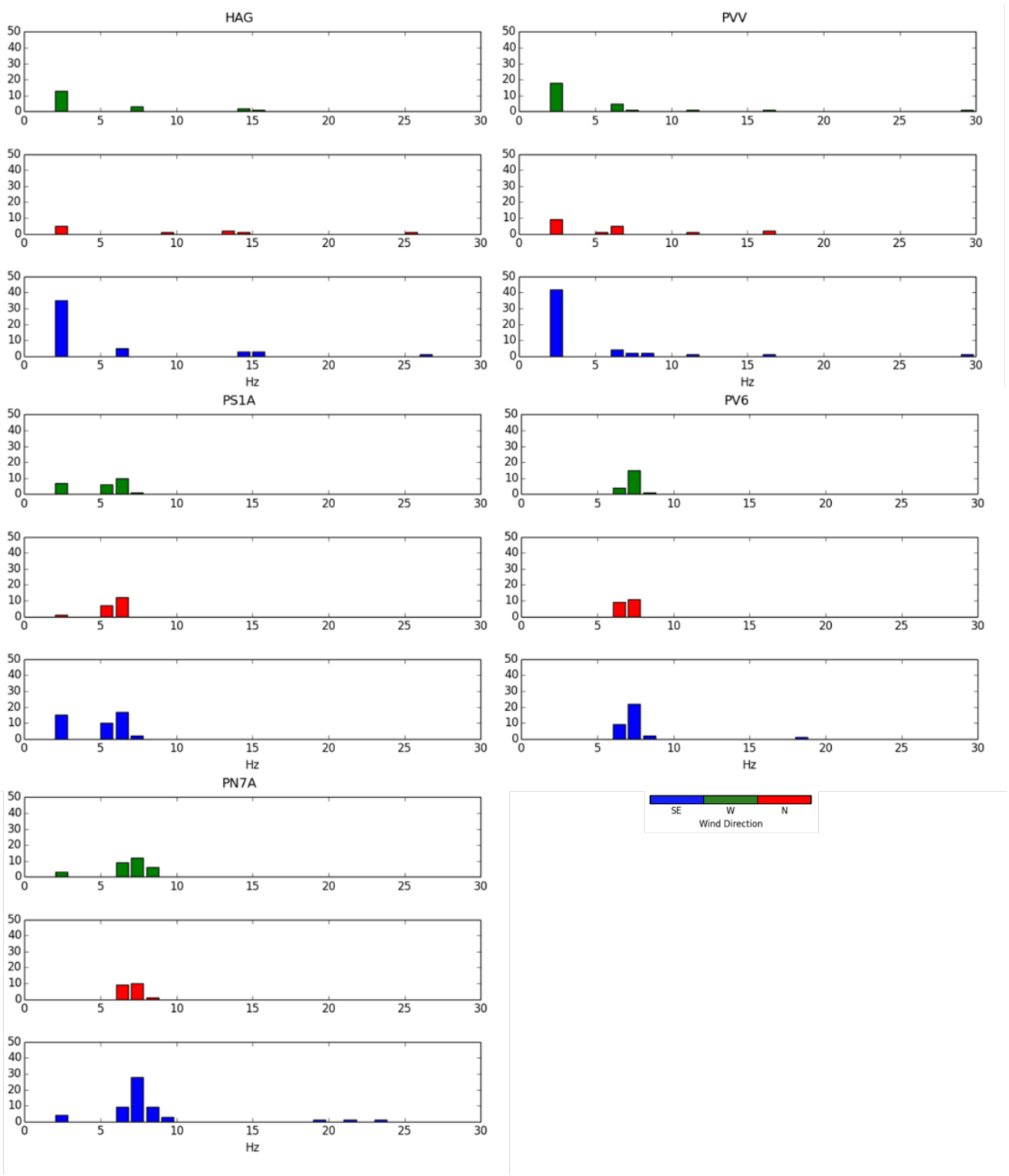

Figure 11: Compilation of main frequency of ground-coupled air wave. At each station the samples are divided by wind direction. The color scale for wind direction is the same across plots and is given above. These plots indicate that the frequency of the ground-coupled air wave is independent of wind direction.

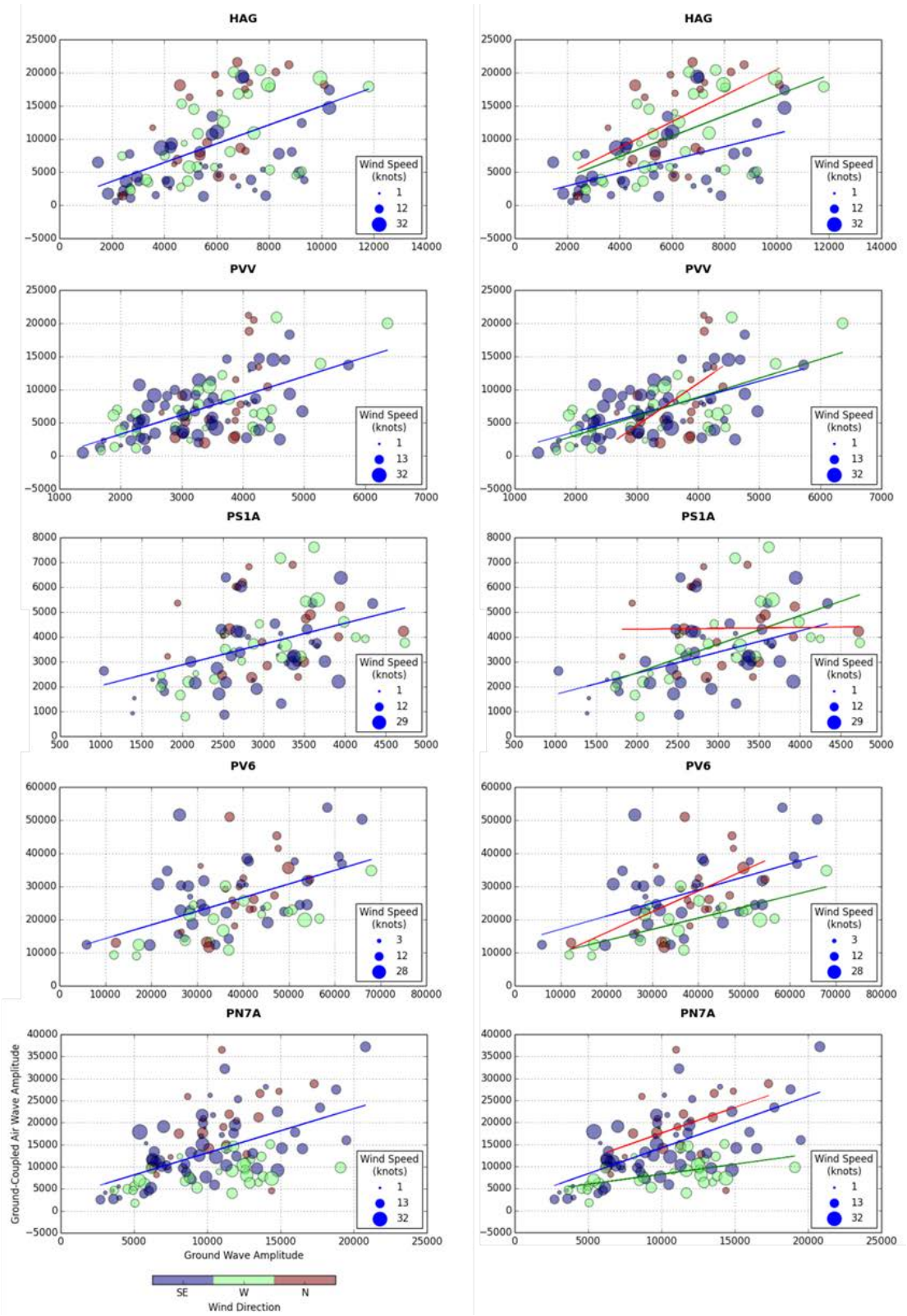

Figure 12: Ground wave and ground-coupled air wave ratios. The left column shows the linear regression for all of the amplitude measurements at the station. The right column shows the linear regressions (color coded to match wind direction) for each wind direction at each station. The R^2 values and slopes for these linear regressions are given in Table 6.

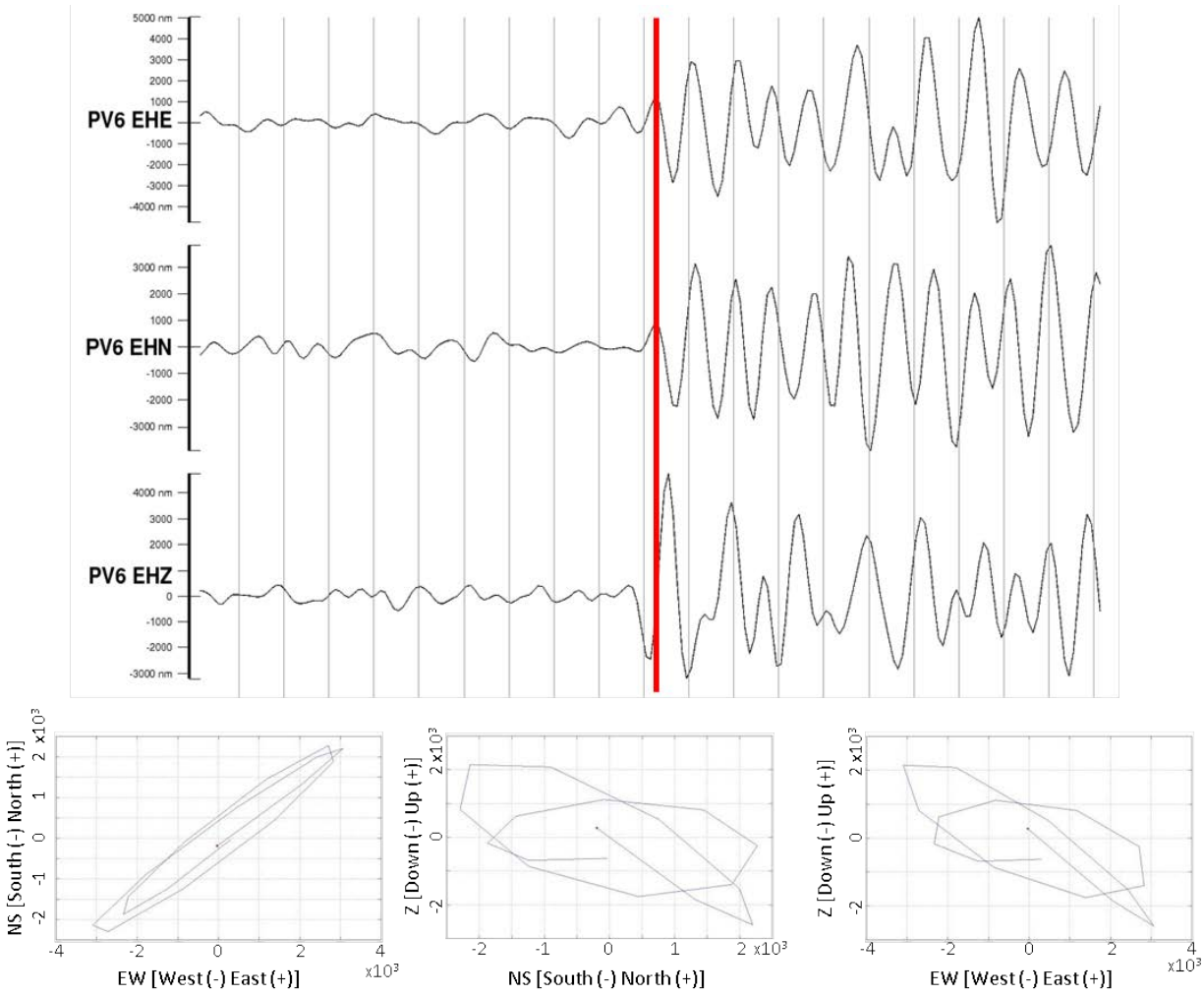

Figure 13: Three components of PV6. The 90^{o} offset between the radial and vertical components is indicative of a Rayleigh wave. The bottom three plots show retrograde elliptical particle motion.

Table 2: Equation Variables

Variable	Definition	Units
v_{lz}	Vertical particle velocity	m/s
p_o	Pressure	Pa
ρ	Density of the ground	kg/m3
α_1	Vertical acoustic wavenumber	1/s
β_1	Vertical wavenumber	1/s
ξ	Horizontal wavenumber	1/s
x	Wavelength	m
t	Period	s
ω	Angular frequency	1/s
W_T	Transverse Transmission Coefficient	-
W_L	Longitudinal Transmission Coefficient	-
P	Pressure	Pa
V	Volume	m^3
E	Energy	J
n	Moles	Moles
R	Gas Constant	$\frac{J}{mole\ K}$
T	Temperature	K

Table 3: Calibration Coefficient. Average ratio (last column) was 5.5 so that was used for our calibration coefficient.

Sample	Pressure Amplitude (Counts)	Pressure from sensor (Pa)	Seismic Amplitude (nm/s)	Seismic Pressure from calculation (Pa)	Ratio (Pressure/Seismic)
1	350	10	25000	1.95	5.13
2	250	7.14	25000	1.95	3.66
3	120	3.43	6000	0.47	7.30
4	140	4	7000	0.5	8
5	60	1.71	5000	0.4	4.28
6	300	8.57	25000	1.95	4.39
7	200	5.71	2000	0.94	6.08

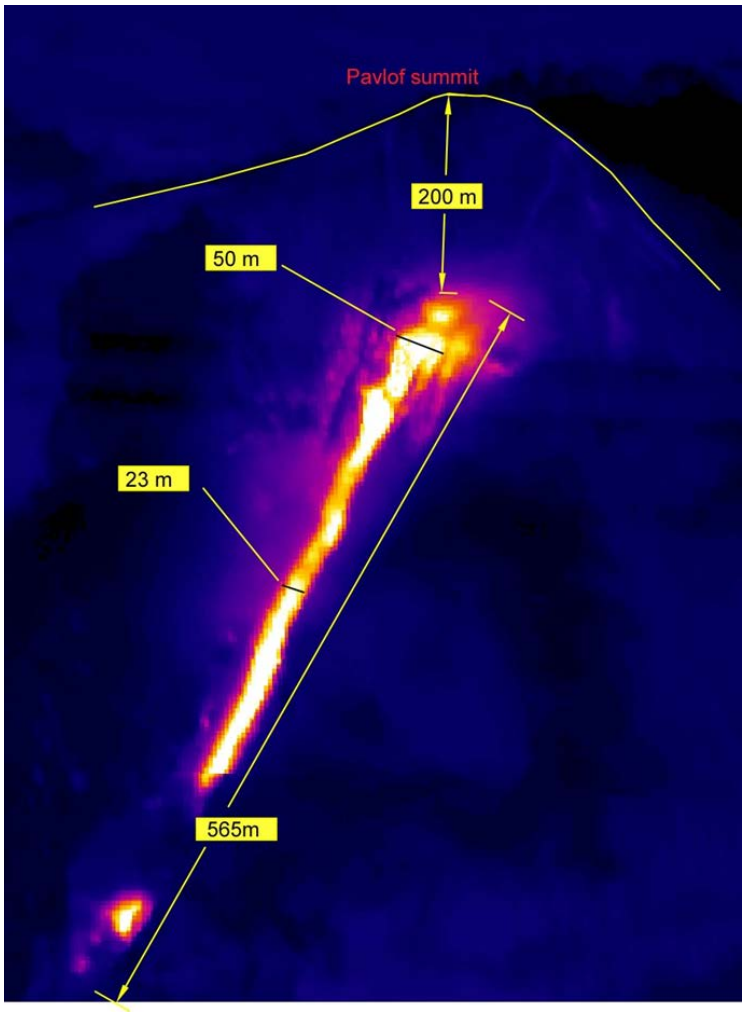

Figure 14: FLIR image of lava flow. This image gives approximate measurements of the lava flow on the southeast face of Pavlof on August 18th. Image from Wessels and Read, Alaska Volcano Observatory/U.S. Geological Survey.

Chapter Four:

Results

The rate of the explosion quakes varied throughout the eruption. There were 31 days of explosion quakes with the first explosion quake on August 14th at 2:54am UTC and the last explosion quake on September 13th at 3:14pm UTC. The maximum number of explosions that occurred in any one day was 5500, the per hour maximum was 350, and the highest number per minute was 19 and occurred on August 19th (fig 7). The rate of explosions per day increased reaching a peak rate per day on August 31st, 18 days into the eruption, and then continued at a decreasing rate for 13 days, forming a distinct peak. In contrast to the per day rates, the per hour plot shows two distinct peaks of activity with one peak showing rates of over 300 explosions per hour at the start of the eruptive phase followed by a slight lull and then another peak of over 300 explosions per hour on Aug 31st. When looking at the rate of explosions per time the period leading up to the peak rate appears to follow an approximately exponential increase. However, at the tail end of the eruption the explosion quakes seemed to suffer a sudden drop off rather than an exponential decay. This suggests that the conduit was being held open by the gas pressure and that when the explosions releasing that pressure stopped that the upper conduit pinched shut.

Plume

The 2007 eruption of Pavlof generated generally weak ash plumes, earning it an official ranking from AVO of VEI 2. The plume was not sustained for long periods of time. As visual

reports and PIREPs indicated the plume was weak, mostly steam, and tended to dissipate rapidly as it was blown south out over the Pacific. This can be seen in both the ASTER and AVHRR images of the plume (fig 15, fig 16). Often there were conflicting viewpoints on if there was a plume or rather if what was seen was just an orographic cloud. The photographic evidence shows that a medium sized plume did in fact develop on August 30th (fig 17). This plume was estimated to reach 20,000 ft (~6 km). This is 12,000 ft (3.6 km) above the 8000 ft (2500 m) summit of the volcano. The maximum heights occur in a six day window that has the highest density of plume reports of any time segment (fig 8). This time window also corresponds well with the peak period of explosion quakes (Aug 28th – September 2nd). During the eruption, plume reports varied to include everything from small summit level ash and steam puffs to the larger plumes seen on August 30th. One regional flight from Cold Bay to Anchorage was cancelled due to ash, indicating that a dangerous level of ash was perceived to be possible.

As discussed earlier, the plume and ash data were gleaned from the AVO eruption logs. Ash was determined to be present in the plume via AVHRR remote sensing as well as reports of lighting in the plume. Lighting occurs in volcanic plumes due to charge differentials, fragmentation of silica rich ash particles, and water/ice interactions (McNutt and Williams, 2010). Due to the inherent variability in reporting styles, units, and precision these data are difficult to analyze (table 4). There are no SO_2 data available, visual reports describe mainly steam and small amounts of ash. The rate of explosions is positively correlated with the number and height of plume reports. Thus, it is reasonable to conclude that there is a connection between the explosion quakes and the gas release and fragmentation processes which result in an ash and gas plume.

Wind

The weather of the Alaskan Peninsula makes effective, on location, monitoring difficult. Pavlof is often cloud covered and storms with high winds are a common occurrence. This makes visual monitoring and verification of ongoing activity challenging. Weather patterns do not affect seismic ground waves, but the state of the atmosphere does have the potential to affect how an explosion quake air wave travels through the air.

The wind data showed a fluctuation in direction, alternating between southeast and west approximately every 48 hours during the first third of the eruption. The wind patterns then changed for around six straight days, consistently blowing from the north, northwest. This pattern change temporally matches the peak eruptive phase – August 27th to September 2nd. Starting on September 2nd the wind direction returned to fluctuating between southeast and west. The wind speeds varied greatly during the eruption from less than 5 knots to greater than 40 knots (fig 18). One knot is equivalent to 0.514 m/s. During the main eruptive peak, and time of highest plume development, the wind was generally less than 15 knots. These speeds are considered to be a moderate breeze or less on the Beaufort Naval scale (Table 5). Starting on September 2nd the wind speeds became more variable and more intense with peak wind speeds reaching gale level designations on September 10th.

By looking into the travel times of the ground-coupled air wave, the effects of wind direction start to become visible (fig 10). Station HAG, which is located south of the vent has a 0.7 second increase in average travel times between when the wind is blowing from the north/northwest (towards the station) and when it is blowing from the southeast (towards the vent). This pattern is repeated with station PVV, located southeast of the vent, where there is a

0.6 second increase between when the wind is blowing from the north/northwest (towards the station) and blowing from the southeast (towards the vent). PS1A is also east-southeast of the vent and shows this same trend, with a 0.5 second increase between north/northwest (towards the station) and southeast (towards the vent). The stations that are located north and west of the vent, PV6 and PN7A show similar commonalities with wind direction and travel time. PN7A is located west-northwest of the vent and shows a 0.4 second increase between winds from the southeast (towards the station) and winds from the west (towards the vent). PV6 echoes this pattern with a time increase of 0.4 seconds between when the wind is blowing from the southeast (towards the station) and when it is blowing from the west (towards the vent).

By comparing these measured values to the theoretical travel times, calculated using the sample periods' average wind speed and direction, we observe that the measured data follows the same pattern of variable arrival times as the calculated data (fig 10). The measured travel time values differ from those calculated by up to a few seconds, with the calculated values being consistently faster than the measured. The largest difference in calculated and measured times occurs on station PV6 with a difference of 2.7 seconds between the calculated and measured travel times for when the wind is coming from the west. This could be the result of topography, the vent is on the southeast side of the edifice, therefore the sound wave would have to travel over or around the summit to reach station PV6, we did not account for the possibility of this additional time in our measurements. Additionally this time difference may be the result of measurement errors, at PV6 the ground-coupled air-wave arrivals occur during the emergent ground wave leading to a smaller amplitude difference and the air wave being more difficult to pick.

Although the absolute travel times vary the between calculated and measured, both of the plots show that when the wind is blowing towards the station the air wave arrives faster and when the wind is blowing away from the station and towards the vent the air wave has a longer travel time. Knowing the effects of wind directions and speeds on travel times is important for future detection and monitoring attempts. Due to availability for this study we only utilized ground based wind measurements. Weather measurements made closer to the volcano and through a variety of altitudes could only enhance the travel time analysis. However, since the stations in this study are close to the vent it is unlikely that the upper atmosphere would affect the waveforms to an appreciable amount.

In addition to understanding travel time variations, it is important to know if the frequency content of the recorded ground-coupled air wave is visibly altered by different wind directions. As can be seen in Fig 11 the main frequency peaks of the ground-coupled air wave do not change with prominent wind direction. The main frequencies recorded vary depending on the station, but do not vary based on wind direction within the same station. Stations PN7A, PV6, and PS1A all show a main frequency concentration between 5 and 10 Hz. Stations HAG and PVV also show frequencies within this band but additionally have both higher 14-16 Hz and lower 2 Hz prominent frequencies as well. These frequencies correspond well to the previous investigation of the 1986 eruption at Pavlof by McNutt et al. (1991) where the ground-coupled air waves were determined to have main frequencies in the 10-15 Hz band. By looking at the entire frequency spectra of the 2007 explosion quakes, it can be noted that spectral content in this band (10-15 Hz) is present at all stations.

Garces et al. (2000) discusses how variations in ground-coupled air wave and ground phase amplitudes might prove useful in seismically monitoring volcanoes. In order to test if these

amplitudes were affected by wind direction or speed the ratio of ground-coupled air wave amplitude and ground wave amplitude were plotted with colors corresponding to wind direction and point size corresponding to wind speed in knots (fig 12). It is possible to determine if there is a relation to wind direction and speed by examining the linear trends of this ratio and the spread of wind speeds. By looking at the entire group of ratios the linear trend R^2 values (the coefficient of determination) for HAG, PVV, PS1A, PV6, and PN7A are 0.28, 0.34, 0.18, 0.25, and 0.27 respectively. There is no discernible pattern between wind direction and higher or lower R^2 values.

Looking at the slopes of the linear regressions, both those calculated from all samples and those determined by wind direction subsets, it is visible that the trends are positive with an increase in ground wave amplitude signaling an increase in air wave amplitude. Looking at the wind direction subset of linear regressions, with the exception of station PS1A, there is a pattern between the wind direction and the slope of the linear regression. The slope of the linear regression is steeper when the wind is blowing towards the station and lower when the wind is blowing away from the station. This shows that when the wind is blowing towards the station a larger amount of energy is being coupled into the ground. The R^2 values and slopes for each linear regression are outlined in table 6. Wind speeds varied between 1 and 32 knots and there is no visible relation between amplitude ratio and wind speed.

Gas

Using the process outlined above the total energy released by Pavlof during the eruption was calculated to be 3.04×10^{11} J. The average explosion released 9.28×10^{6} J of energy, equivalent to the blast generated by 2.22 kg of TNT.

The plume generated at Pavlof was considered to be mainly composed of steam. By making the assumption that all gas released was water the total metric tons of water released by the eruption was calculated to be 729 metric tons of water. The average amount of water released per explosion was 0.022 metric tons, which is equivalent to 22 liters or 4.84 gallons of water per explosion. Assuming a lava with 4 wt % water and a density of 2.9 tons/m^3 this amount of water release is equivalent to fully degassing 6284 m^3 of lava. In our calculations there is a direct relationship between temperature and the number of moles of water calculated. Since we used a constant temperature value (630^o Celsius), based on one observation on August 18th, for the entire eruption it is possible that this value could be an underestimate if the temperature was actually cooler or an overestimate if the temperature of the magma was hotter over the course of the eruption. More temperature data would allow for a better understanding of this value.

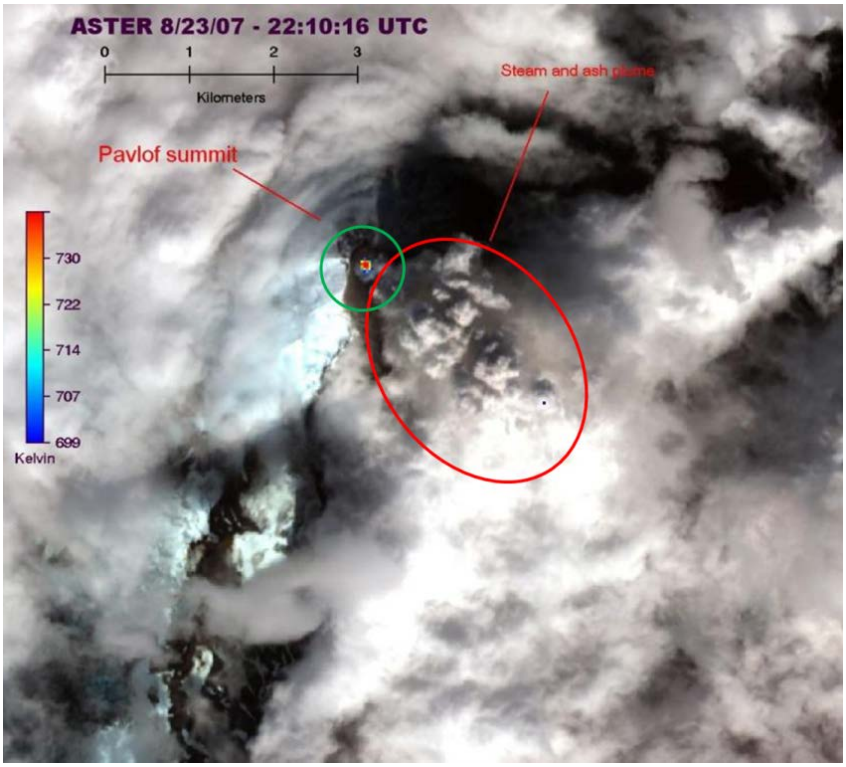

Figure 15: ASTER satellite image. The plume is visible within the red ellipse. A thermal anomaly is also visible within the green circle. Image edited from Wessels, Alaska Volcano Observatory/U.S. Geological Survey.

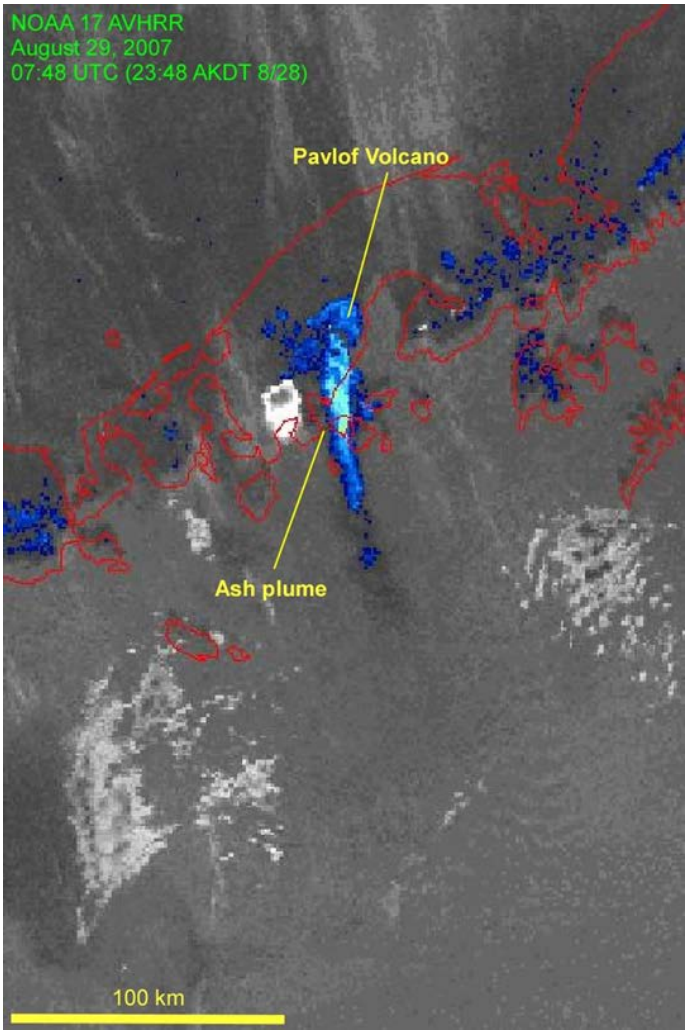

Figure 16: AVHRR satellite image. The ash plume can be seen in this image as the blue streak, it is being blown south over the Pacific Ocean, visibly extending to almost 100 km in length. Image from Wessels, Alaska Volcano Observatory/U.S. Geological Survey.

Figure 17: August 30th plume. It reached an altitude of 18,000 ft. Image from Waythomas, Alaska Volcano Observatory/U.S. Geological Survey.

Table 4: Plume Descriptions. Descriptions of the log entries used to create Figure 8, showing the lack of consistency in reporting style which makes this type of information difficult to analyze. Used with permission of the Scientist-in-charge of AVO, J. Power

Date	Height	Description	Method
Aug 15th	8000 ft (summit level)	Black 'smoke' extending 2 nautical miles SE of volcano at 10 knots	PIREP
Aug 15th	-	No plume later in the day	Visual
Aug 18th	Few hundred m above flank surface	Dilute ash cloud	Photo
Aug 18th	-	Sizable steam plume	Photo
Aug 23rd	13120 ft asl	Small steam and ash	ASTER
Aug 23rd	Couple thousand feel above summit	Anemic thin stripe of ash	Visual
Aug 23rd	18000 ft	Mile wide plume blowing towards SE	PIREP
Aug 27th	-	8 pixel anomaly	Satellite
Aug 28th	16000 ft	Ash cloud travelling SSE	PIREP
Aug 28th	14000 ft	Ash moving SE	PIREP
Aug 28th	20000 ft+	Large black plume moving ESE	Visual
Aug 28th	-	Large plume	Visual
Aug 29th	14000 ft	Plume	PIREP
Aug 29th	-	Ash no longer visible on satellite	Satellite
Aug 29th	14000 ft	Spewing ash	PIREP
Aug 29th	15000 ft	Steam / light ash trailing ESE for 10 nautical miles	PIREP
Aug 30th	17-18000 ft	Eruption plume	Photo
Aug 30th	8000 – 15000 ft	Diffuse ash cloud moving SE	PIREP
Aug 30th	8000 – 15000 ft	Ash is low level and dissipating as it drifts SE at 20 knots	SIGMET
Aug 30th	8000 – 15000 ft	Minor low level eruption, Ash drifting SE over water	PIREP, Satellite
Aug 30th	8000 – 15000 ft	Ash drifting SE over water at 20 knots	PIREP, Satellite
Aug 30th	8000 – 15000 ft	Ash cloud diffuse and difficult to see on satellite	PIREP, Satellite
Aug 30th	20000 ft	-	PIREP, Satellite
Aug 30th	20000 ft	Plume, lighting, increased explosions	Photo
Aug 30th	17-18000 ft	Robust steam plume with ash at base	Photo
Aug 31st	-	Mentioned in ASH advisory	-
Aug 31st	12000 ft	Ash cloud drifting ESE for 10 miles	PIREP
Aug 31st	12000 ft	Ash moving SE at 10 knots	SIGMET
Sep 1st	13000 ft	Eruption cloud	ASTER VNIR
Sep 1st	20000 ft	Weak Ash	AVHRR
Sep 4th	-	Plume not moving while other clouds move past, no ash signal detected, cloudy	AVHRR

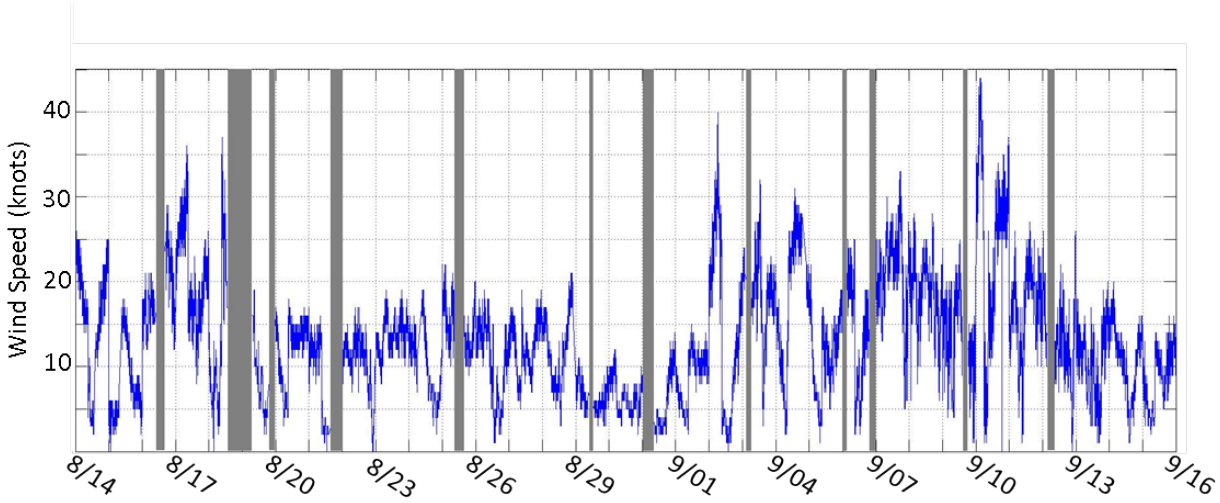

Figure 18: Wind speed each minute. Velocity is in knots. The vertical grey bands are periods of time where there are no wind speed data from Cold Bay.

Table 5: Beaufort Wind Scale. Created by Sir Francis Beaufort of the U.K. Royal Navy in 1850 and still in use by NOAA.

Wind (knots)	Classification
<1	Calm
1-3	Light Air
4-6	Light Breeze
7-10	Gentle Breeze
11-16	Moderate Breeze
17-21	Fresh Breeze
22-27	Strong Breeze
28-33	Near Gale
34-40	Gale
41-47	Strong Gale
48-55	Storm
56-63	Violent Storm
64+	Hurricane

Table 6: R^2 Values and Slopes for Amplitude Ratio Plots. Spaces shaded blue are where the wind is blowing from the vent towards the station. Spaces shaded red are where the wind is blowing from the station towards the vent.

Station	Measurement	Total	North/Northwest	Southeast	West
HAG	R^2	0.28	0.29	0.25	0.33
PVV	R^2	0.34	0.32	0.34	0.44
PS1A	R^2	0.18	0.0003	0.22	0.36
PV6	R^2	0.25	0.29	0.25	0.49
PN7A	R^2	0.27	0.20	0.42	0.27
HAG	Slope	1.42	1.97	0.99	1.54
PVV	Slope	2.91	6.34	2.54	2.87
PS1A	Slope	0.84	0.03	0.85	1.15
PV6	Slope	0.41	0.63	0.39	0.34
PN7A	Slope	1.0	1.16	1.17	0.45

Chapter Five:

Discussion

Explosion quakes are easily distinguishable from other seismic events due to their abrupt high amplitude and high frequency signal that is offset between stations based on distance from the source. The explosion quakes that occurred during the 2007 eruption at Pavlof occurred at a rate previously unseen from this volcano. The maximum number of explosion quakes noted during the real time monitoring effort was 14 explosion quakes per minute (S. McNutt, written communication). The maximum number of explosion quakes manually counted during this study increased this number to a recorded 19 explosion quakes per minute. Rates of up to 16 explosions per minute were recorded during the vigorous Strombolian I phase of the 1999 eruption of Shishaldin, showing that although our rate is high it is not unprecedented (Thompson et al., 2002).

Continuous Seismicity

RSAM (Real-time Seismic Amplitude Measurement) is commonly used in monitoring circumstances due to its ability to simplify complex, rapidly occurring seismic data into an easier to comprehend plot of average amplitude (Endo and Murray, 1991). This average amplitude plot can be used to see general trends in seismic activity, with an increase in different types of seismicity, such as tremor, there is an overall increase in the average amplitude of the trace. We compared RSAM data to the explosion quake rate and to wind speed (fig 19). For this plot we

calculated the RSAM for station HAG. At this station there was the largest time gap between the ground wave and the ground-coupled air wave, therefore the amplitude of the explosions would not be hidden by interference with the ground wave. This allows the RSAM to be calculated from both the ground and ground-coupled air wave amplitudes rather than the interference pattern of the two. Looking at this overlay it is easy to see that as the number of explosion quakes ramps up at the start of the eruption that the RSAM follows a similar trend. This is a logical pattern to see since RSAM measures the average amplitude and explosion quakes have high amplitude onsets. As the number of explosion quakes increase the average amplitude over the same period of time would be expected to increase as well. The similarity in trend between RSAM and explosion quake rate continued through both peaks of the main eruptive phase of August 27th-September 1st.

Starting on September 2nd the similarity between RSAM and explosion quakes is less apparent. On September 2nd the rate of explosion quakes rapidly dropped off and then fluctuated in rate while RSAM values show some decrease from the main peak but remain high overall. The decrease on September 7th can be attributed to the fact that on this day three of the seismometers, including HAG, were non-functioning for a total of approximately 11 hours intermittently throughout the day. At the end of the eruption the explosion quakes went from hundreds per day to less than 25 per day showing as a near vertical drop off in the data. RSAM however shows an additional period of increase on September 11th, a day with very few explosion quakes, before it starts steadily declining.

This difference in RSAM and explosion quakes during the second half of the eruption, most notably September 2nd-4th, and September 8th-9th, and September 11th, can be attributed to volcanic tremor. Even though the explosions themselves have high amplitude ground waves, if

the tremor that occurs between the explosive phases also has high amplitude then the non-discriminatory RSAM average will remain high. It is therefore possible to conclude that the tremor had relatively low amplitude during the start of the eruption resulting in RSAM values tracking with explosion quake rates. The tremor amplitude then increased and remained high during the second half of the eruption, overshadowing any changes in explosion quake amplitudes before tapering down at the end of the eruption.

This systematic change in explosion and tremor amplitude shows that there was likely a change in magma or gas supply to the surface resulting in less explosive events. For explosions to occur there must be a continued gas flux. A steady supply of gas enriched magma would allow for high rates of explosions while a lessening of magma supply would lessen explosive activity (Garces and Hansen, 1998). This then leads to the conclusion that the high amplitude tremor that is keeping the RSAM values high is not solely dependent on bubble production. There is no consensus in the scientific community of the exact cause of volcanic tremor. It is commonly thought to occur as a source effect from bubble formation and subsequent collapse (McNutt et al., 1991). As the drop in explosive quakes indicates less gas reaching the surface it is then possible to determine that this instance of tremor is likely being produced from a different mechanism such as magma resonance or induced fracturing occurring deeper in the conduit, unrelated to the explosions occurring at the vent interface (Garces and McNutt, 1997).

The second plot in this figure shows the RSAM values plotted against the wind speed. In this plot we see that when the wind speed is high the RSAM is low (August 14^{th} – 18^{th} and September 10^{th} – 12^{th}) and reversely that when the wind speed is low that the RSAM is high (August 29^{th} – September 2^{nd}). Wind can appear as noise on a seismogram and create amplitude changes. However due to the fact that the wind speed was highest at the start and end of the

eruption and lowest during the peak of the eruption it is more plausible that these RSAM trends are caused from actual seismic events rather than a change in wind noise.

Wind

By looking at the ground-coupled air waves recorded travel times, frequencies, and amplitude ratios in relation to wind direction and speed it is possible to determine to what extent these atmospheric effects must be monitored when utilizing ground-coupled air waves. The travel time differences show that the wind directions and speeds play a role in how long the air-wave takes to travel from vent to station. Therefore the common wind directions and speed ranges for the volcano of interest should be known in order to effectively program an automated explosion monitoring program. However, the frequency content of the ground-coupled air waves does not show the same variation with wind direction. Therefore the frequency is not an aspect of the seismic record that requires adjusting due to wind interference. Note that theoretical reflection and transmission coefficients are not frequency dependent, in agreement with our observations.

For the amplitude ratio between the ground-coupled air wave and the ground phase there is a positive linear trend throughout all of the data, and within the binned wind directions themselves, however there is not a clear connection between the R^2 values of the linear trends and the wind direction in relation to station location. Therefore, because the wind speed and direction does not affect the coefficient of determination it can be assumed that the overall positive trend between ground and air-wave amplitudes will remain constant despite variable weather conditions. The slopes of the linear regressions show that in the majority of cases if the wind is blowing towards the station that the slope will be larger than if the wind is blowing away

from the station. This indicates that overall the ratios have a consistently positive linear trend where the wind direction may enhance or diminish the scale of the positive trend but does not alter the coefficient of determination (R^2) of the data sets. The amplitude ratios were also inspected in relation to wind speed and there does not appear to be any visual correlation between wind speed and amplitude ratio. Since it is overall a positive linear trend one can use either or both ground wave amplitude or air wave amplitude for monitoring the explosivity.

Therefore it can be assumed that when using ground-coupled air waves for volcanic monitoring the only seismological aspect that is affected and must be accounted for is the travel time of the air wave. This is a factor that can easily be accounted for in future detection codes. Frequency and amplitude do not appear to be altered. This allows for them to be used in an uncorrected state for further analysis, such as the energy and mass flux calculations. Additionally the unaffected linear relationship between the seismic ground wave amplitude and the ground-coupled air waves amplitude may be used in future studies to better understand magmatic gas content (Garces et al. 2000).

Gas

Due to the mass flux being directly derived from the energy calculation, the cumulative release plots for both of these variables follow the same shape (fig 20). Both the energy and gas fluxes are directly connected to the activity of magma within the conduit system. Therefore by examining the cumulative release curve it is possible to make some inferences on the magma behavior within the conduit. Figure 20 is divided a-g to show the sections described as follows. The plot begins with an exponential increase in events (a). This rapid increase could indicate the first batch of magma being injected and degassing. The plot then takes on a linear trend during

the middle section (August 30th - September 2nd) where the highest rates and plume heights were noted (b). This linear trend indicates that the supply of gas/magma was constant. After this main phase there is a flattening of the curve followed by another small increase(c-d), which is then repeated (e-f), before the plot flatlines rapidly at the end of the explosive phase of the eruption (g). This flattening followed by increase pattern could represent additional small batches of magma that ascended and degassed before the end of the eruption.

On figure 20 we have also plotted the cumulative number of explosion quake events over the course of the eruption. This curve also follows the same pattern as the energy and mass flux curves. This shows that although it is useful to know the amount of energy and water being released that during a fast-paced monitoring situation it is not necessary to go through the calculations and determine the exact values of energy and gas. It would be possible to gain an understanding of the general trends of these properties simply by examining the cumulative event curve.

Energy

Yokoyama (1957) lists five different categories in which a volcano exerts energy. They are: 1) volcanic tremor, 2) local earthquakes, 3) fracturing of the surrounding ground material 4) ejection of material, and 5) producing disturbances in the atmosphere or ocean. He further subdivides the ejection of material into potential, kinetic, and thermal energies. Yokoyama (1957) focuses his paper on the thermal subcategory stating that it constitutes the largest proportion of energy emitted (De la Cruz-Reyna, 1991). Therefore the magnitude of the total energy erupted can be determined by the magnitude of thermal energy (Shimozuru, 1967). Table

7 gives the thermal energies calculated by Yokoyama (1957) and the VEIs (Simkin et al., 1981) for several eruptions of varying scale.

The 2007 eruption of Pavlof was labeled as a VEI 2 eruption by the Alaska Volcano Observatory. The energy calculations made in this paper are from the pressure and volume of a bubble bursting and are therefore kinetic energy values. Other forms of volcanic kinetic energy include tremor and volcano-tectonic (VT) earthquakes (Shimorzuru, 1967). The total kinetic energy release calculated from the explosion quakes was 3.04×10^{11} J. This is several orders of magnitude smaller than the smallest energy for a VEI 2 eruption listed by Yokoyama (1957), which is 1×10^{14} J for the 1893 eruption of Azumasan. This equates to approximately 0.3% of the thermal energy release for a similar VEI volcano. Although it is only a small proportion, by following Yokoyama's (1957) theory that acoustic kinetic energy is only considered to make up a small portion of total energy release when compared to thermal energy, we can deem this result as consistent with prior observations.

Pavlof is in a remote area, suffers from perpetually bad weather, low visibility, and has frequent eruptions (McNutt, 1986). The ability to track these characteristic explosions, calculate the kinetic energy released, monitor the eruptive intensity, and track potential ash plume development from the seismic dataset, is promising for future monitoring of eruptive events, as well as an increased understanding of seismic verses acoustic efficiency.

Mass

The average gas mass released per bubble is 0.022 metric tons, which is 0.022 m^3 of water per bubble. The maximum bubble mass is 0.2 metric tons, or 0.2 m^3 of water. When compared to other Strombolian eruption calculated bubble gas masses (Vergniolle et al., 2004),

these values are low. However, the Pavlof eruption was a notably gas poor eruption, with no SO_2 measurements (airborne measurements were not done and no SO_2 was detected in Ozone Monitoring Instrument data), and only a small plume (Waythomas et al., 2008). It is speculated by Waythomas et al., (2008) that the 2007 eruption might have been the result of a leftover slug of partially degassed magma from the eruption of 1996 having finally worked itself to the surface.

In order to determine if our calculated mass of gas release is reasonable we compare it with the total mass of ejecta to determine a total weight percent water released. Our calculated 729 metric tons of water is equivalent to 729×10^3 kg of water. Waythomas et al. (2008) calculated a total ejected volume of 10^5 m^3. Using a density of 2.9×10^3 kg/m^3 for basaltic andesite we get a weight percent water of 0.025 wt % being exsolved during the eruption. Since not all water is exsolved from the magma during an eruption - as evidenced by lava samples commonly having measureable weight percents of water and with weight percents of arc basaltic andesites ranging from 1-6 wt % - having a 0.025 wt % of water exsolved during eruption is a reasonable amount, especially for an eruption of this size with small plume development (Winter, 2010; Chouet and Matoza, 2013). This small amount of exsolved gas suggests that other methods of gas release must be operating, these include passive exsolution at the vent-air interface, exsolution into porous ground material before the gas reaches the vent-air interface, and that some of the water might stay dissolved in the lava after expulsion.

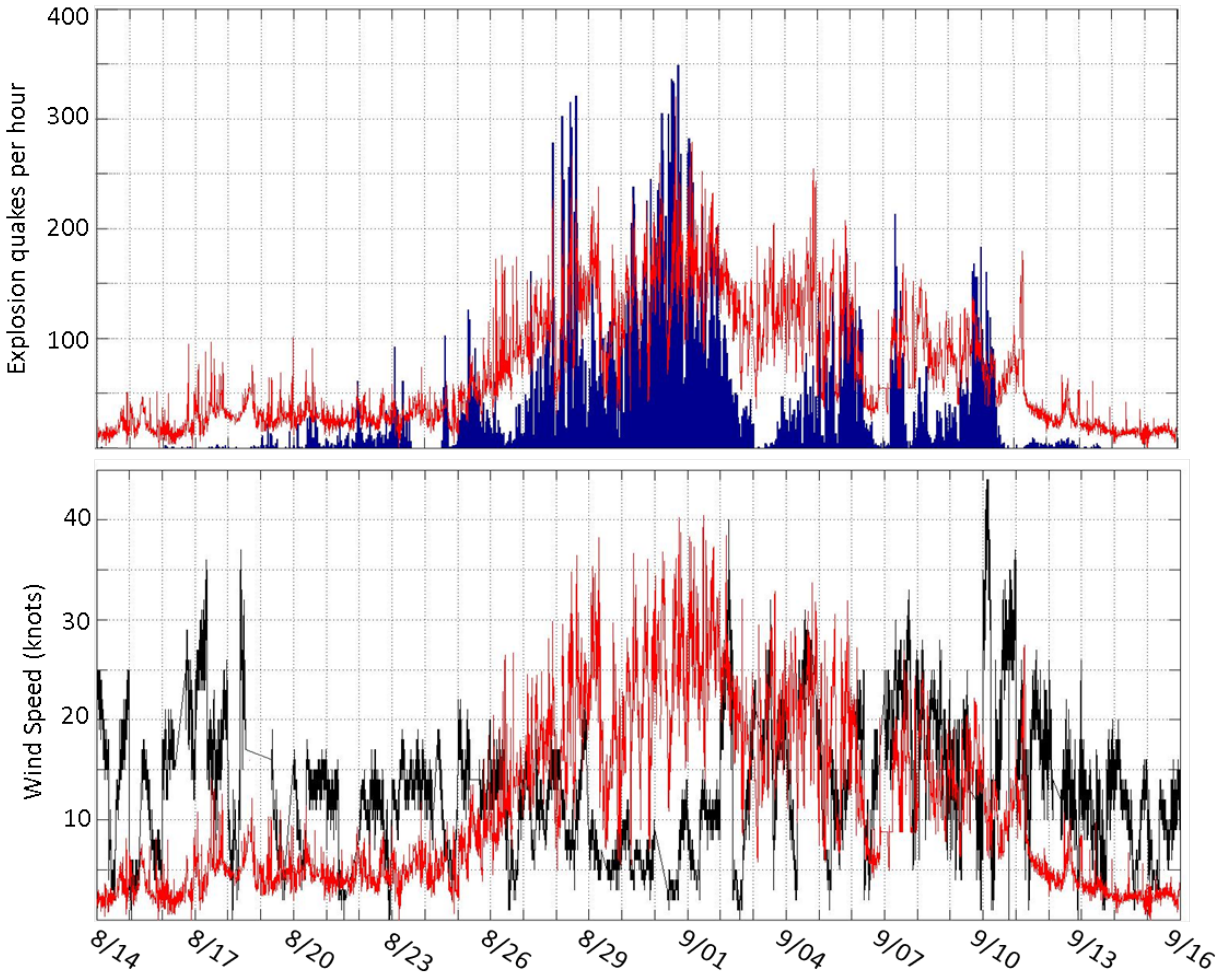

Figure 19: RSAM, explosion rates, and wind speed. The red line is the 1-minute RSAM value calculated for station HAG. The RSAM values have been shifted down by 120 counts in order to better facilitate large scale pattern relationships between the plots. The top plot shows the RSAM compared with the per hour rates of explosions. The bottom plot shows the RSAM compared with the wind speed in knots.

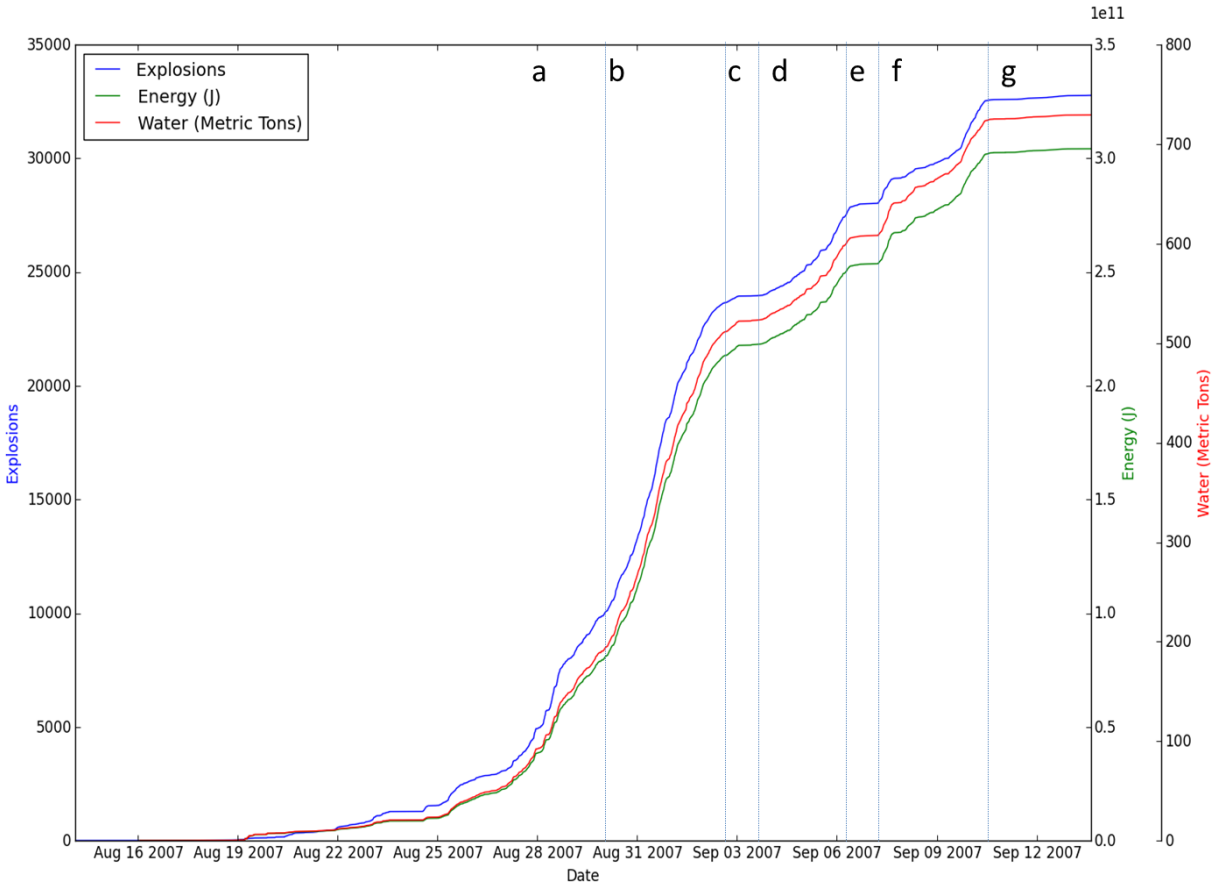

Figure 20: Cumulative explosion quakes, energy and water mass. The calculated cumulative value curves for explosion rates and energy released, mass of water exsolved by Pavlof, as calculated from ground-coupled air wave explosion amplitudes and Garces et al. (2000) equations. The labeled divisions (a-g) are in reference to the discussion in the text.

Table 7: Thermal Energy Release. Spaces shaded yellow are VEI 2 eruptions, log energies (in ergs) from Yokoyama 1957, VEIs from Simkin et al 1981. Chart modified from De la Cruz-Reyna 1991

Volcano	**Year**	**Log E (ergs)**	**Joules**	**VEI**
Mihara	1912	20.80	6.31E+13	1
Sakurazima	1946	24.32	2.09E+17	2
Torishima	1939	23.99	9.77E+16	2
Mihara	1950	23.97	9.33E+16	2
Miyakeshima	1940	23.68	4.79E+16	2
Pemtang Bata	1933	22.65	4.47E+15	2
Azumasan	1893	21.00	1.00E+14	2
Mihara	1777	24.00	1.00E+17	3
Guuntur	1843	22.81	6.46E+15	3
Asama	1935	22.68	4.79E+15	3
Una Una	1898	22.26	1.82E+15	3
Adatarasan	1900	21.81	6.46E+14	3
Asama	1938	21.60	3.98E+14	3
Sakurazima	1914	25.66	4.57E+18	4
Asama	1783	24.94	8.71E+17	4
Fugi	1707	24.85	7.08E+17	4
Komagatake	1929	23.75	5.62E+16	4
Bandaisan	1888	23.00	1.00E+16	4
Krakatoa	1883	25.00	1.00E+18	6
Tambora	1815	26.92	8.32E+19	7

Chapter Six:

Conclusions

De Angelis et al. (2012) states that "volcano monitoring efforts should not rely primarily on second-order phenomena such as air-to-ground coupling." Despite their arguments that ground-coupled air waves from explosion quakes should only be used in the planning of future infrasonic arrays, this study proves that there is value in utilizing these less conventional seismic signals. Although infrasonic records are a more direct measure of the atmospheric pressure there is not the same level of infrastructure for infrasound for there is for seismic data. Until De Angelis et al.'s (2012) goal of a complete infrasonic array covering the Aleutians is realized, knowing how to use the seismic equivalent has value. Additionally, the small scale explosions that were recorded by the Pavlof seismic array are not large enough to be captured by a regional rather than local infrasound array.

Another situation that calls for recognition of the usefulness of these less commonly used signals is financial. The funding situation at the Alaska Volcano Observatory has been effectively halved in recent years due to smaller federal budgets and the sequestration (Witze, 2013). With less financial support available monitoring techniques must become more creative. The likelihood of the ideal and expansive infrasonic network becoming a reality in the near future is slim. In fact many of the currently deployed seismic networks have begun to go offline as expensive maintenance trips become financially unfeasible. Thus the maximum use must be made of existing data and infrastructure.

The benefit of the ground-coupled air wave is that even small scale explosions are detected and require a minimum of only 2 stations at different distances to the volcano to detect the slower atmospheric wave velocities. Therefore, even if several seismic stations go offline, as long as two still function it is possible to calculate the volcano's energy/gas mass flux. The effect of stations going offline and not being repaired was realized during the 2013 eruption of Pavlof. During this eruption the data analysis suffered because two of the local stations, PN7A and PV6, were offline (Waythomas et al., 2014). Pavlof erupted twice in 2014, the first episode was from May to June and only two of the seismic stations, PN7A and PV6 were functioning throughout. The other four stations (PS4A, PVV, PS1A, and HAG) suffered a data outage and have no record of this eruption. The second eruptive episode of 2014 occurred in November and all six stations were operational throughout. No published research has yet been done on either of these 2014 eruptive periods so it is unknown how damaging the station data outage during the first eruptive period will be to research.

Having the ability to calculate kinetic energy, mass release, and knowing the relationship between these values and the cumulative explosion rate enables the monitoring community to make better informed decisions for both nearby residents and the avionics community. The fact that the cumulative curves for energy, gas mass flux, and event count follow the same trends increases the value of monitoring explosion quakes. Even without calculating the gas and energy one can still determine their trend through the event count. By being able to track and calculate these parameters from the seismic records we show the multi-functionality of seismic monitoring at a time when the entire monitoring community must learn to do more with less. In this study we were able to utilize the seismically recorded ground-coupled air wave to calculate reasonable numbers for both kinetic energy release and gas mass release resulting from the Strombolian

explosions during the 2007 eruption of Pavlof. We further show that explosion-quake rate follows both energy and gas release rates. Therefore, by monitoring the explosion-quake rate, monitoring communities will be able to have a better understanding of magmatic gas flux and the potential for ash plume development.

References

AAWU. (2015). Volcanic Ash Advisory Center. from http://vaac.arh.noaa.gov/vaac_info.php

AVO. (2007). Pavlof Response Log.

AVO. (2014). Alaska's Volcanos Introduction - How Many Volcanoes in Alaska? , from http://www.avo.alaska.edu/volcanoes/about.php

Braun, T., & Ripepe, M. (1993). Interaction of Seismic and Air Waves Recorded at Stromboli Volcano. Geophysical Research Letters, 20(1), 65-68.

Brekovskikh, L. M. (1980). Waves in Layered Media (R. T. Beyer, Trans.). New York: Academic Press.

Chouet, B. A., & Matoza, R. S. (2013). A multi-decadal view of seismic methods for detecting precursors of magma movement and eruption. Journal of Volcanology and Geothermal Research, 252, 108-175.

De Angelis, S., Fee, D., Haney, M., & Schneider, D. (2012). Detecting hidden volcanic explosions from Mt. Cleveland Volcano, Alaska with infrasound and ground-coupled air waves. Geophysical Research Letters, 39(L213312). doi: 10.1029/2012GL053635

De la Cruz-Reyna, S. (1991). Poisson-distributed patterns of explosive eruptive activity. Bulletin of Volcanology, 54, 57-67.

DeMets, C., Gordon, R. G., Argus, D. F., & Stein, S. (1990). Current plate motions. Geophys. J. Int, 101, 425-478.

Endo, E. T., & Murray, T. (1991). Real-time seismic amplitude measurement (RSAM): a volcano monitoring and prediction tool. Bulletin of Volcanology, 53(7), 533-545.

Garces, M. A. (1997). On the volcanic waveguide. Journal of Geophysical Research, 103(B10), 22,547-522,564.

Garces, M. A., & Hansen, R. A. (1998). Waveform analysis of seismoacoustic signals radiated during the Fall 1996 eruption of Pavlof volcano, Alaska. Geophysical Research Letters, 25(7), 1051-1054.

Garces, M. A., & McNutt, S. R. (1997). Theory of the airborne sound field generated in a resonant magma conduit. Journal of Volcanology and Geothermal Research, 78, 155-178.

Garces, M. A., McNutt, S. R., Hansen, R. A., & Eichelberger, J. C. (2000). Application of wave-theoretical seismoacoustic models to the interpretation of explosion and eruption tremor signals radiated by Pavlof volcano, Alaska. Journal of Geophysical Research, 105(B2), 3039-3058.

Grewingk, C. (1850). Beltrag zur Kentniss der orographischen und geognostischen Beschaffenhelt der Nordwest Kuste Amerikas, mit den anllegenden Inseln. Russ. K. min. Gesell Verb. St. Pteresburg, 204, 50-53.

Hagerty, M. T., Schwartz, S. Y., Garces, M. A., & Protti, M. (2007). Analysis of seismic and acoustic observations at Arenal Volcano, Costa Rica, 1995-1997. Journal of Volcanology and Geothermal Research, 101, 27-65.

Haney, M. M., van Wuk, K., Preston, L. A., & Aldridge, D. F. (2009). Observation and modeling of source effects in coda wave interferometry at Pavlof Volcano. The Leading Edge, Special Section: Seismic Modeling, 554-560.

Johnson, J. B., Aster, R. C., Ruiz, M. C., Malone, S. D., McChesney, P. J., Lees, J. M., & Kyle, P. R. (2003). Interpretation and utility of infrasonic records from erupting volcanoes. Journal of Volcanology and Geothermal Research, 121, 15-63.

Johnson, J. B., & Lees, J. M. (2000). Plugs and chugs - seismic and acoustic observations of degassing explosions at Karymsky, Russia and Sangay, Ecuador. Journal of Volcanology and Geothermal Research, 101, 67-82.

Johnson, J. B., Lees, J. M., & Gordeev, E. I. (1998). Degassing Explosions at Karymsky Volcano, Kamchatka. Geophysical Research Letters, 25(21), 3999-4002.

Johnson, J. B., & Malone, S. D. (2007). Ground-Coupled acoustic air waves from Mount St. Helens provide constraints on the May 18, 1980 eruption. Earth and Planetary Science Letters, 258, 16-31.

Kennedy, G. C., & Waldron, H. H. (1955). Geology of Pavlof Volcano and Vicinity Alaska. Geological Survey Bulletin, 1028-A.

McGimsey, R. G., Neal, C. A., Dixon, J. P., Malik, N., & Chibisova, M. (2011). 2007 Volcanic activity in Alaska, Kamchatka, and the Kurile Islands: Summary of events and response of the Alaska Volcano Observatory. U.S. Geological Survey Scientific Investigations Report 2010-5242, 110.

McNutt, S. R. (1986). Observations and Analysis of the B-Type Earthquakes, Explosions, and Volcanic Tremor at Pavlof Volcano, Aslaska. Bulletin of the Seismological Society of America, 76(1), 153-175.

McNutt, S. R. (1999). Eruptions of Pavlof Volcano, Alaska, and their Possible Modulation by Ocean Load and Tectonic Stresses: Re-evaluation of the Hypothesis Based on New Data from 1984-1998 Pure and Applied Geophysics, 155, 701-712.

McNutt, S. R. (2014). [PN7A Pressure Sensor].

McNutt, S. R., & Beavan, R. J. (1981). Volcanic earthquakes at Pavlof Volcano correlated with the solid earth tide. Nature, 294(5842), 615-618.

McNutt, S. R., & Jacob, K. H. (1986). Determination of Large-Scale Velocity Structure of the Crust and Upper Mantle in the Vicinity of Pavlof Volcano, Alaska. Journal of Geophysical Research 91(B5), 5013-5022.

McNutt, S. R., Miller, T. P., & Taber, J. j. (1991). Geological and seismological evidence of increased explosivity during the 1986 eruptions of Pavlof volcano, Alaska. Bulletin of Volcanology, 53, 86-98.

McNutt, S.R., G. Thompson, J. Johnson, S. De Angelis, and D. Fee, Seismic and Infrasonic Monitoring, Chapter 63 of Encyclopedia of Volcanoes, 2nd Edition, Sigurdsson, H., B. Houghton, S.R. McNutt, H. Rymer, and J. Stix (eds.), Elsevier, 2015, in press.

McNutt, S. R., Tytgat, G., Estes, S. A., & Stihler, S. D. (2010). A Parametric Study of the January 2006 Explosive Eruptions of Augustine Volcano, Using Seismic, Infrasonic, and Lightning Data. USGS Professional Paper, 85-102.

McNutt, S. R., & Williams, E. R. (2010). Volcanic lightning: global observations and constraints on source mechanisms. Bulletin of Volcanology. doi: 10.1007/s00445-010-0393-4

Minster, J. B., & Jordan, T. H. (1978). Present-day plate motions. Journal of Geophysical Research: Solid Earth (1978-2012), 83(B11), 5331-5354.

Neal, C., Girina, O., Senyukov, S., Rybin, A., Osiensky, J., Izbekov, P., & Ferguson, G. (2009). Russian eruption warning systems for aviation. Nat. Hazards, 51, 245-262.

Neal, C. A., Casadevall, T. J., Miller, T. P., Hendley II, J. W., & Stauffer, P. H. (2004). Volcanic Ash-Danger to Aircraft in the North Pacific. U.S. Geological Survey Fact Sheet 03-97. from http://pubs.usgs.gov/fs/fs030-97/

NOAA. (2008). Welcome to the Anchorage Center Weather Service Unit. from http://cwsu.arh.noaa.gov/

Petersen, T., & McNutt, S. R. (2007). Seismo-acoustic signals associated with degassing explosions recorded at Shishaldin Volcano, Alaska, 2003-2004 Bulletin of Volcanology. doi: 10.1007/s00445-006-0088-z

Reyes, C. G., & West, M. E. (2011). The Waveform Suite: a robust platform for manipulating waveforms in MATLAB. Seismological Research Letters, 82(1), 104-110.

Ripepe, M. (1996). Evidence for gas influence on volcanic seismic signals recorded at Stromboli. Journal of Volcanology and Geothermal Research, 70, 221-233.

Ripepe, M., Poggi, P., Braun, T., & Gordeev, E. (1996). Infrasonic waves and volcanic tremor at Stromboli. Geophysical Research Letters, 23(2), 181-184.

Roach, A. L., Benoit, J. P., Dean, K. G., & McNutt, S. R. (2001). The combined use of satellite and seismic monitoring during the 1996 eruption of Pavlof volcano, Alaska. Bulletin of Volcanology, 62, 385-399.

Sabatier, J. M., Bass, H. E., & Bolen, L. N. (1986). Acoustically induced seismic waves. J. Acoust. Soc. Am., 80(2), 646-649.

Shimozuru, D. (1967). Discussion on the Energy Partition of Volcanic Eruption. Paper presented at the 14th General Assembly of IUGG, Symposium on Physical Volcanology, Zurich.

Simkin, T., Siebert, L., McClelland, L., Bridge, D., & Newhall, C. (1981). Volcanoes of the world: a regional directory, gazetteer, and chronology of volcanoes during the last 10,000 years. Smithsonian Institution, Washington, 1-233.

Thompson, G., McNutt, S. R., & Tytgat, G. (2002). Three distinct regimes of volcanic tremor associated with the eruption of Shishaldin Volcano, Alaska 1999. Bulletin of Volcanology, 62, 535-547.

Vergniolle, S., Boichu, M., & Caplan-Auerbach, J. (2004). Acoustic measurements of the 1999 basaltic eruption of Shishaldin volcano, Alaska 1. Origin of Strombolian activity. Journal of Volcanology and Geothermal research, 137, 109-134.

Vergniolle, S., & Brandeis, G. (1994). Origin of the sound generated by Strombolian explosions. Geophysical Research Letters, 21(18), 1959-1962.

Vergniolle, S., & Brandeis, G. (1996). Strombolian explosions 1. A large bubble breaking at the surface of a lava column as a source of sound. Journal of Geophysical Research, 101(B9), 20,433-420,447.

Vergniolle, S., Brandeis, G., & Mareschal, J. C. (1996). Strombolian explosions 2. Eruption dynamics determined from acoustic measurements. Journal of Geophysical Research, 101(B9), 20,449-420,466.

Waythomas, C. F., Haney, M. M., Fee, D., Schneider, D. J., & Wech, A. (2014). The 2013 eruption of Pavlof Volcano, Alaska: a spatter eruption at an ice-and snow-clad volcano. Bulletin of Volcanology. doi: 10.1007/s00445-01400862-2

Waythomas, C. F., Miller, T. P., & Mangan, M. T. (2006). Preliminary Volcano Hazard Assessment for the Emmons Lake Volcanic Center, Alaska. In U. S. G. S. (Ed.), Scientific Investigations Report. Anchorage, Alaska.

Waythomas, C. F., Prejean, S. G., & McNutt, S. R. (2008). Alaska's Pavlof Volcano Ends 11-Year Repose. EOS, Transactions, American Geophysical Union, 89(23), 209,211.

Winter, J. D. (2010). Principles of Igneous and Metamorphic Petrology (2nd ed.): Pearson Higher Ed.

Witze, A. (2013). Financial blow for Alaskan volcano monitoring. Nature. doi: 10.1038/nature.2013.13041

Yokoyama, I. (1956). Energetic in Active Volcanoes 2nd Paper. Bull. Earthq. Res. Inst., XXXV.

Appendix A:

Station Pseudo-Helicorders

The following pseudo-helicorder images were created using the dbheli command in the software package Antelope, distributed by Boulder Real Time Technology. Each line is one day (24 hours) in length. They all start at midnight on August 14th and end at midnight on September 16th 2007. This large format view of the eruption allows broad trends and mechanical issues to be seen more clearly. The lahar sequences that flowed down the southeast slope are clearly visible on PVV. The mechanical issue with PS1A during the first week of the eruption is also very visible.

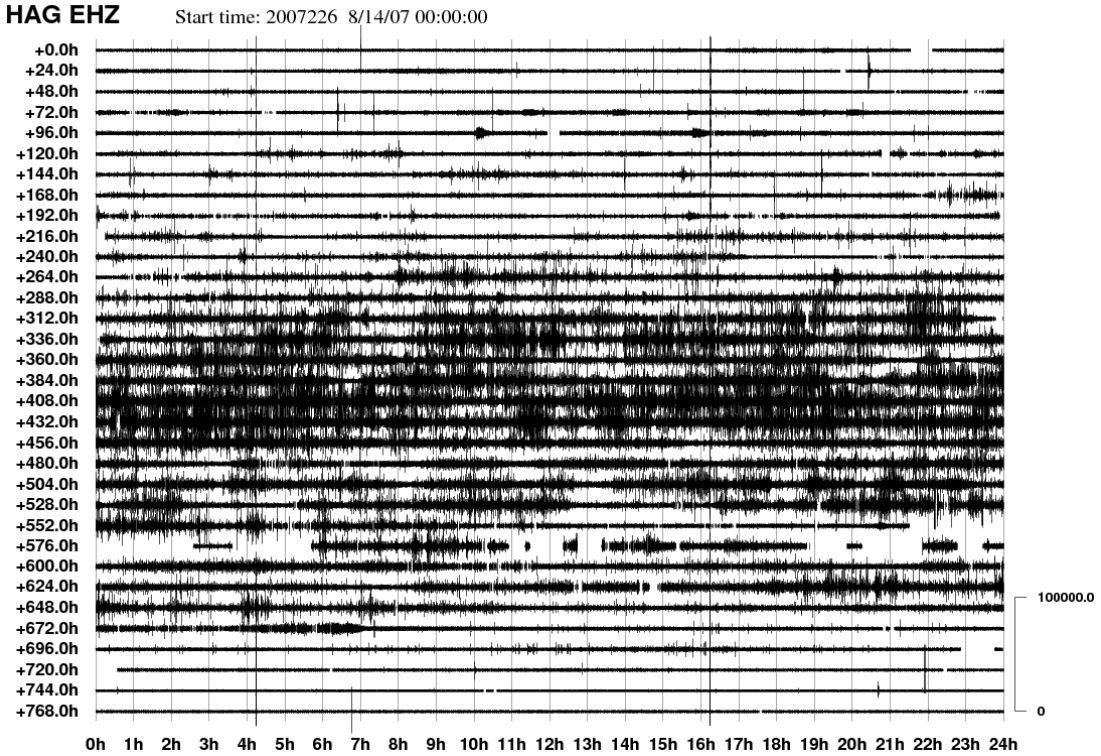

Figure A1: HAG pseudo-helicorder

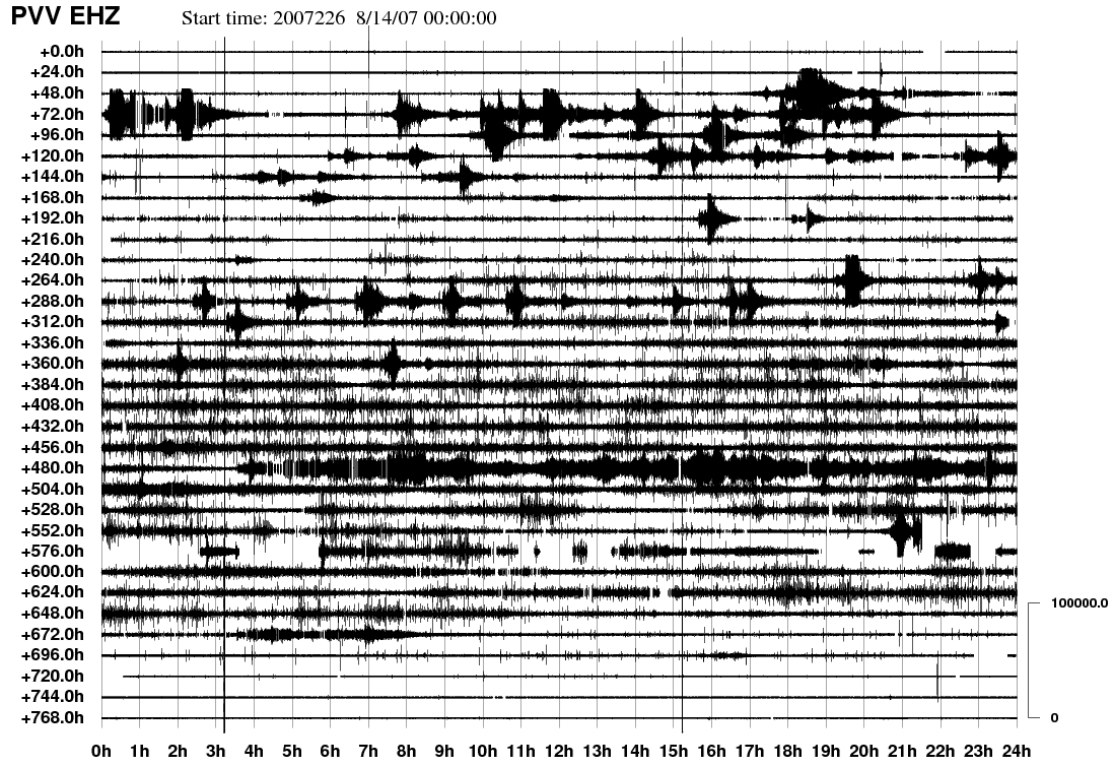

Figure A2: PVV pseudo-helicorder

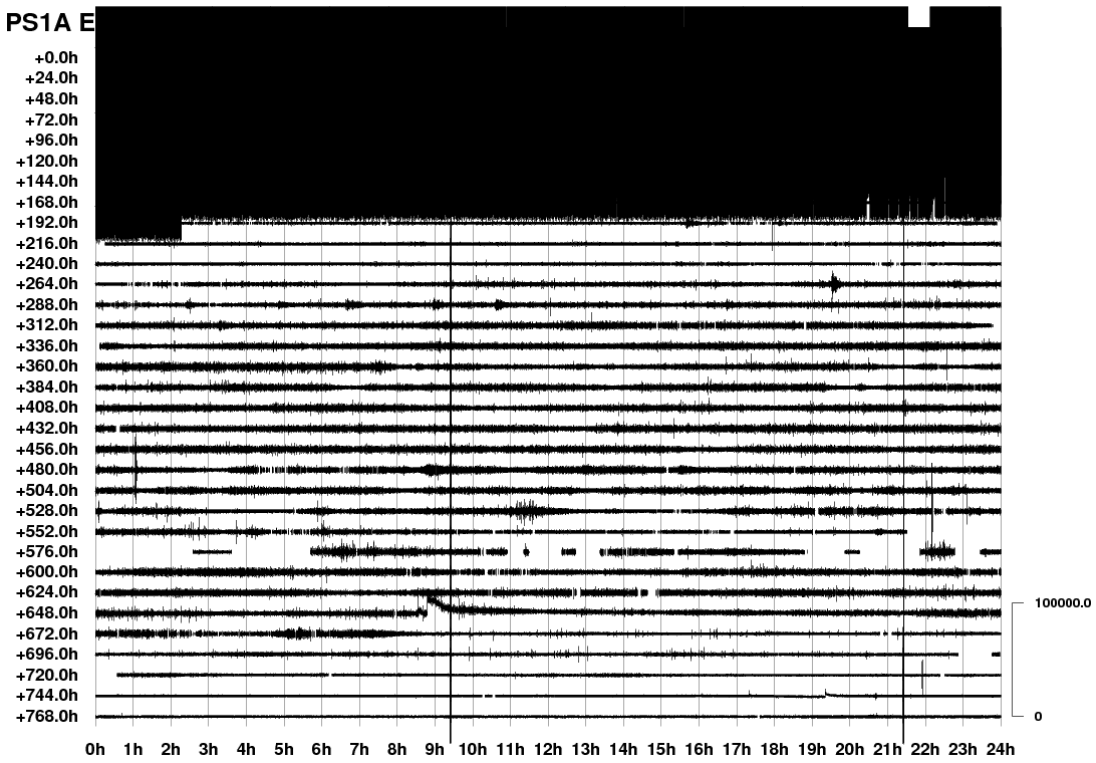

Figure A3: PS1A pseudo-helicorder

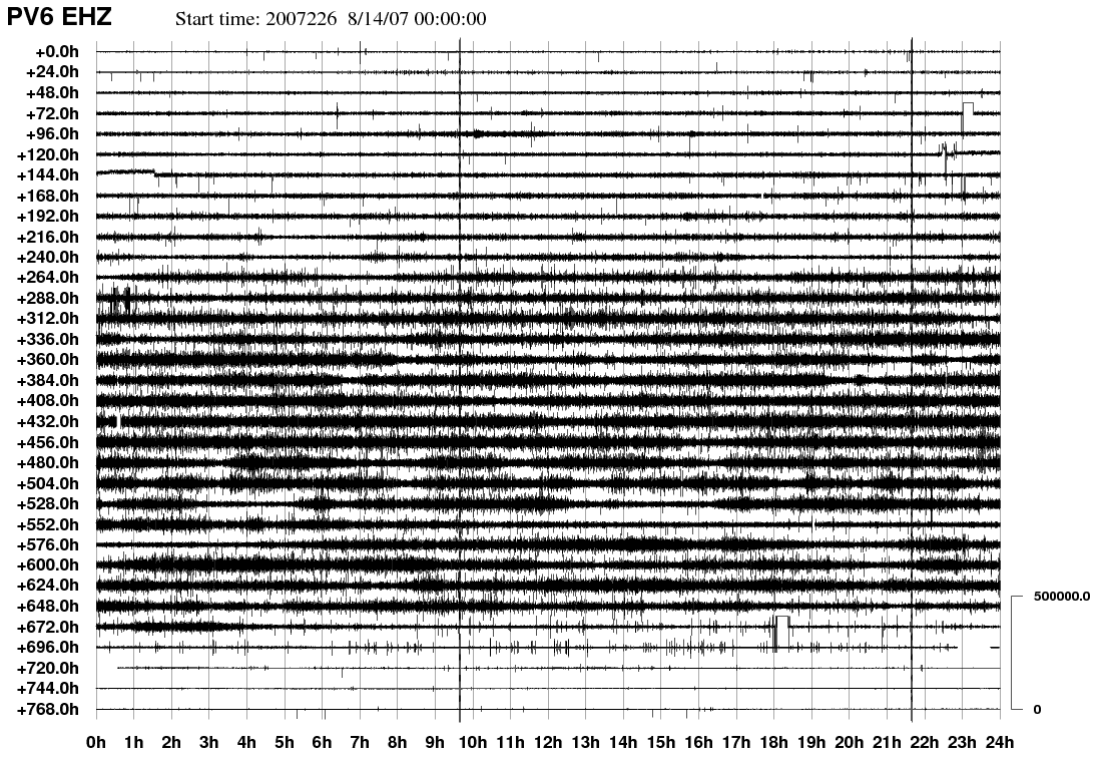

Figure A4: PV6 pseudo-helicorder

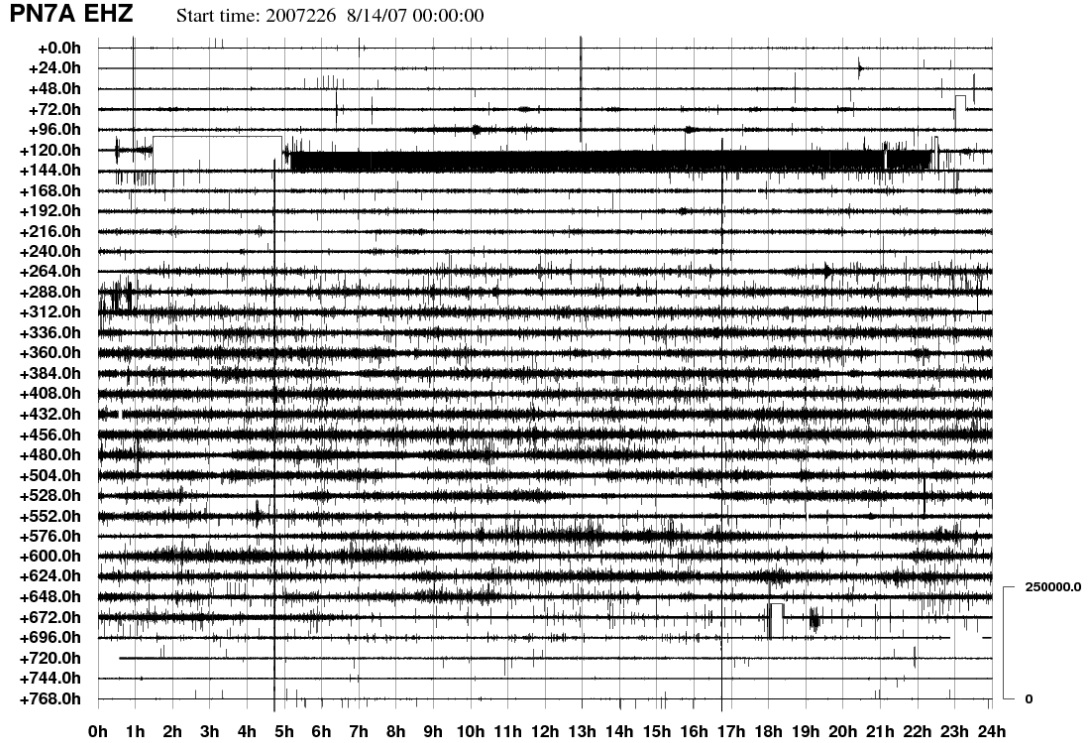

Figure A5: PN7A pseudo- helicorder

Appendix B:

MATLAB Code for Recording Ground-Coupled Air Wave Amplitudes

This MATLAB code is used to take the manually recorded times from the input file and pick and record the amplitudes for each seismic trace. This code applies a human error correction of 0.5 seconds and takes into account the calculated wind direction travel time difference from average values. The code works by going to the station and time specified and then shifting between traces, moving backwards or forwards in time according to air wave travel time differences between stations, and then taking the maximum amplitude within a window determined by the human error and travel time differences. These values are then recorded into a file. During the manual recording of events only the clearest time and station were recorded. Therefore in order to calculate all of the amplitudes this code must be altered and run one time for each station that had a manually recorded event, for a total of 5 runs. The result files are then compiled in order to have a complete list of amplitude measurements.

```
function stats = AmpsAllAttempt_retry()
   %AmpsAllAttempt
   % Cassandra Smith & Glenn Thompson, 2014

   load ArrivalsDividedbyStation.mat
   % first row is a header row, so start at index 2
   MIN_INDEX = 2;

   % create a datasource object
   dbpath = '/home/c/cmsmith10/dbpavlof2007_224_273';
   ds = datasource('antelope', dbpath);

   chan = 'EHZ';
   network = 'AV';
   location = '--';
```

```
%triggers based on assumed potential human error of +-0.5s + wind delay calculations
%wind delay [sta(wd in sec)]: HAG(0.7), PN7A(0.4), PS1A(0.5), PV6(0.4), PVV(0.6)

% structure of stations, trigger values, and arrival data files
s(1).station = 'HAG';
s(1).pre_trigger = 1.2;
s(1).post_trigger = s(1).pre_trigger;
s(1).arrivals = ArrivalsHAG;
s(1).differential_travel_times = 0;
s(2).station = 'PN7A';
s(2).pre_trigger = 0.9;
s(2).post_trigger = s(2).pre_trigger;
s(2).arrivals = ArrivalsPN7A;
s(2).differential_travel_times = 12.2;
s(3).station = 'PS1A';
s(3).pre_trigger = 1;
s(3).post_trigger = s(3).pre_trigger;
s(3).arrivals = ArrivalsPS1A;
s(3).differential_travel_times = 5.6;
s(4).station = 'PV6';
s(4).pre_trigger = 0.9;
s(4).post_trigger = s(4).pre_trigger;
s(4).arrivals = ArrivalsPV6;
s(4).differential_travel_times = 20.0;
s(5).station = 'PVV';
s(5).pre_trigger = 1.1;
s(5).post_trigger = s(5).pre_trigger;
s(5).arrivals = ArrivalsPVV;
s(5).differential_travel_times = 8.3;

% Let's loop over all stations
for station_index = 1:length(s)

   sta = s(station_index).station;
   arrival = s(1).arrivals(MIN_INDEX:end) -
s(station_index).differential_travel_times;
   pre_trigger = s(station_index).pre_trigger;
   post_trigger = s(station_index).post_trigger;

   % ****
   % Compute the predicted arrival times of air waves using arrival
   % time of this station and the differential_travel_times defined
   % for this station

   for i=MIN_INDEX:length(arrival)
```

```
                epoch_start = arrival(i) - pre_trigger;
                epoch_end   = arrival(i) + post_trigger;

                % create a scnl object
                scnl = scnlobject(sta, chan, network, location);

                % get our waveform object
                snum = epoch2datenum(epoch_start);
                enum = epoch2datenum(epoch_end);
                w = waveform(ds, scnl, snum, enum);

                if isempty(w)
                   continue
                end

                m = max(abs(detrend(w)));
                if ~(m>0)
                   m = 0;
                end

                if (length(m)==1 & length(arrival(i)==1))
                   stats(i-1) = struct('sta', sta, 'chan', chan, 'snum', snum, 'enum', enum,
'arrival_time', arrival(i), 'max_amp', m);
                else
                   disp(sprintf('length m=%d',length(m)));
                   disp(sprintf('length arrival_time=%d', length(arrival(i))));
                   error('Aborting')
                end

             end

                   figure(1);      % Plot station subplots of time of event and maximum amplitude
recorded
             subplot(2,3,station_index)

             length([stats.arrival_time])
             length([stats.max_amp])
             plot( epoch2datenum([stats.arrival_time]), [stats.max_amp], 'k.' )
             datetick('x')
             title(sprintf('%s Amplitudes',sta))
             xlabel('date')
             ylabel('amplitude (nm)')

          end

       end
```

Appendix C:

Equations for Pressure Code

The following equations are required for equation (1) and come from Brekhovskikh (1980)

Reflection Coefficient

$$V = \frac{Z_L cos^2 2\gamma_1 + Z_T sin^2 2\gamma_1 - Z}{Z_L cos^2 2\gamma_1 + Z_T sin^2 2\gamma_1 + Z}$$

Longitudinal Transmission Coefficient

$$W_L = -\frac{c_1}{c}\frac{\cos\theta \cos 2_{\gamma 1}}{\cos\theta_1}(V-1)$$

Transverse Transmission Coefficient

$$W_T = \frac{2sin^2\gamma_1}{\tan\theta}(V-1)$$

Impedances

$$Z = \frac{\rho c}{\cos\theta} \qquad Z_L = \frac{\rho_1 c_1}{\cos\theta_1} \qquad Z_T = \frac{\rho_1 b_1}{\cos\gamma_1}$$

Table C1: Variables for Pressure Code

Symbol	Description
θ	Angle normal to wave front
θ_1	Angle for longitudinal wave front
γ_1	Angle for transverse wave front
ρ	Density of the ground
W_T	Transverse Transmission Coefficient
W_L	Longitudinal Transmission Coefficient
c	P wave velocity in air
c_1	P wave velocity in unconsolidated ground tephra
b_1	S wave velocity in unconsolidated ground tephra
Z	Normal Impedance
Z_T	Transverse Impedance
Z_L	Longitudinal Impedance

Appendix D:

Python Code for Calculating Energy and Mass Release from Amplitudes

The following is the Python code that we wrote to calculate the energy and gas mass release of the explosion quakes. The code and its variables are explained in Chapter Three: Procedures and Methodology. It is provided here for completeness, the files listed in the code as input and output are provided in table form after the code.

```
#Set Up needed modules

import numpy as np
import matplotlib.pyplot as plt
import csv
from netcdftime import num2date
from datetime import datetime

#-----------------------------------------------------------------------------------------------------
#import amplitude file

date, Amp = np.loadtxt('Amps_for_demo.txt', usecols = (0,1), unpack=True)
datez = np.loadtxt('Amps_for_demo.txt', usecols = (0,))

#-----------------------------------------------------------------------------------------------------
#set up variables

theta = 76.61 #angle normal to sound wavefront
theta1 = 13.39 #angle for longitudinal wavefront
y1 = 13.39

r2 = 7060. #distance of PN7A from vent

#values from Garces et al 2000
p = 1. #air density kg/m3
p1 =  2700. #ground density kg/m3
c = 320. #speed of pwave in air m/s
c1 = 1500. #speed of pwave in ground loose tephra shallow m/s
```

```
	b1 = 380. #s wave velocity surface loose tephra m/s

	#assume an average frequency of 7Hz for the ground coupled air wave at PN7A,
determined from freq plots
	f = 7.

	#-----------------------------------------------------------------------------------------------
	#variables to determine

	Ampt = Amp*0.000000001 #convert amplitude from nm/s to m/s

	B = (2*np.pi*f)/b1 #vertical wavenumber (used speed of s in loose tephra)
	kaC = (2*np.pi*f)/c1 #horizontal wavenumber (used speed of p in loose tephra)
	x = (c/f) #wavelength
	t = (1.0/f) #period
	w = 2*np.pi*f #angular freq
	a1 = (2*np.pi*f)/c #vertical acoustic wavenumber (used speed of p in air bc acoustic
wave)

	j = 1j

	#-----------------------------------------------------------------------------------------------
	#solve for the Zs and Ws and V

	# Impedences
	Z_T = (p1*b1)/np.cos(y1)
	Z_L = (p1*c1)/np.cos(theta1)
	Z = (p1*c)/np.cos(theta)

	#print 'Z_T:', Z_T
	#print 'Z_L:', Z_L
	#print 'Z:', Z

	#V is the reflection coefficient
	V = ((Z_L*(np.cos(2*theta)**2)) + (Z_T*(np.sin(2*theta)**2)) -
Z)/((Z_L*(np.cos(2*theta)**2)) + (Z_T*(np.sin(2*theta)**2)) + Z)

	#W_L and W_T ar the longitudinal and transverse transmission coefficients
	W_L = (-c1/c)*((np.cos(theta)*np.cos(2*y1))/np.cos(theta1))*(V-1)
	W_T = (2*(np.sin(y1)**2)/np.tan(theta))*(V-1)

	#-----------------------------------------------------------------------------------------------

	#solved for po
	po = (Ampt*p1*w)/((-a1*W_L*np.exp(-j*a1))+(kaC*W_T*np.exp(-
j*B)))*np.exp((kaC*x)-(w*t))
```

```
	po_r = np.real(po) #real portion
	pop_r = abs(po_r) #absolute value/magnitude of real portion

	pop_rff = pop_r*5.5 #(absolute value, real portion multiplied by multiplicative coefficient)

	#-----------------------------------------------------------------------------------------------
	# use pressure volume to get n moles
	wavelength = c/f
	r1 = wavelength/4. #radius of original bubble = 1/4 period = rise time, also used as initial radius for pressure calc

	Vol = (4./3.)*np.pi*(r1**3) #(m3 using 1/4 period as radius, sphere at vent)

	R = 8.3145 #(J/mole*K)
	T_C = 630. #http://www.avo.alaska.edu/images/image.php?id=13477 temperature from FLIR
	T = T_C + 273. #in K

	pop_rff_amped = pop_rff*(r2/r1) #pressure amplified by 1/r law back to what the source pressure would be

	n = (pop_rff_amped*Vol)/(R*T)

	Energy = pop_rff_amped*Vol

	mE = np.mean(Energy)
	#print mE

	#-----------------------------------------------------------------------------------------------
	#convert from number of moles to metric tonnes - assuming gas released is water

	# 1 mole = 18 grams for H2O
	grams = n*18

	#1kg = 1000g
	kg = grams*0.001

	#1 metric tonne = 1000000grams
	metric_tonnes = grams*0.000001

	mmt = np.mean(metric_tonnes)
	#print mmt

	#-----------------------------------------------------------------------------------------------
```

```
        #convert matlab datenum to python datetime
        #
http://nbviewer.ipython.org/github/nicolasfauchereau/UoA_Workshop_14082014/blob/master/Scipy.ipynb

        matlab_datenum = datez

        date_proleptic = num2date(matlab_datenum, units='days since 000-01-00 00:00:00', \
                        calendar='proleptic_gregorian')

        #---------------------------------------------------------------------------------------------------

        #write results to a file

        p2r = (zip(date, date_proleptic, Energy, metric_tonnes))
        f = open('FLUX_FILE_Demo.txt', 'w')
        writer = csv.writer(f, delimiter='\t')
        writer.writerow(('datenum', 'date', 'Energy', 'metric_tonnes H2O'))
        writer.writerows(p2r)

        cs = np.cumsum(metric_tonnes)
        cs_en = np.cumsum(Energy)
        #---------------------------------------------------------------------------------------------------
```

Table D1: Example of Input File. The file should be a tab delimited text file containing two columns and no header line. The first column should have the datenum value for the time of the explosion quake. The second column should have the measured amplitude of the event in nm/s. The code is easily altered to accommodate for other set ups of the data.

733274.6509	3605.051647
733286.3656	3120.143774
733290.867949	11621.839879

Table D2: Example of Output File. This file will be a tab delimited text file and can be customized to contain any of the intermediary calculated values.

Datenum	Date	Energy	Metric tons H2O
733274.65090000001	2007-08-20 15:37:18	6219117.1217189394	0.014909990024757068
733286.36560000002	2007-09-01 08:46:28	5382596.8299943581	0.012904478798483035
733290.86794899998	2007-09-05 20:49:51	20048973.067421038	0.048066306292563872

Appendix E:

Effect of Wind Noise on Ground-Coupled Air Wave Picks

Introduction

For this study we manually inspected the seismograms with no frequency filter. By doing the manual inspection we were able to record more explosion quakes than Haney et al., (2009) were able to do with their detection algorithm, and more than were noticed during the 24 hour/day monitoring of the eruption by AVO. However, even with our manual inspection it is possible that due to wind noise that smaller explosions might have been missed.

Methods

In order to determine the extent that wind noise interference might have on manually recognizing ground-coupled air waves we compared two hour segments from a calm day and a windy day. We determined if the day was calm or windy by looking at the plot of wind speed. We choose August 30th from noon to 2:00 pm as the calm portion, during this time winds did not exceed 10 knots. For the windy portion we picked September 10th from midnight to 2:00 am where the wind speeds reached 44 knots. We attempted to pick portions of the record where there were no data drop outs.

We used the original explosion counts and then filtered the resulting data with a 10-20 Hz band pass filter applied through dbpick in the software package Antelope. We choose this filter based on the work of McNutt et al. (1991) who noted the frequency range of 10-15 Hz being

prominent on all stations. In our frequency analysis the prominent energy was most often between 5-10 Hz. However all stations did have components in the 10-15 Hz range as well. The 10-20 Hz band pass was chosen after some testing that showed that this range both limited the noise and allowed for easy identification of the explosion quakes. After filtering we manually counted the ground-coupled air waves.

Results

The results of this experiment show there was an increase in visible explosion quakes on both the calm and the windy day. By calculating the percent increase in number over each section we saw an increase of 27 % in the calm section and 60 % in the windy section.

Table E1: Effect of Noise and Filters on Explosion Quake Counts

Date	Calm	Windy	Events Unfiltered	Events Filtered	Percent Change
8/30	X		182	231	26.9%
9/10		X	232	372	60.3%

Conclusions

The difference in percentage increase shows that wind noise is likely playing a part in hiding these events, as wind noise would be frequencies above and below the filter frequencies. However, it must also be considered that the extraneous noise in the seismograms might be from tremor, which would also be filtered out as it has a frequency below the filtered band. Either way, the large increase in discovered explosion quakes shows the potential of these events in monitoring. Haney et al. (2009) detected a maximum of 300 explosion quakes per day with their cross correlation of the ground waves algorithm. In this study we increased this number to a maximum of 550 explosion quakes per day by manually counting the ground-coupled air waves.

The potential of even more explosion quakes being detected with optimal frequency filtering further increases the potential for these events to be used in effective monitoring. Therefore, for future analysis of explosion quakes a band pass filter in this range should be applied during monitoring/processing to catch these small events that get lost in the wind noise so that they can be incorporated into the analysis.

Below is a set of pseudo-helicorders showing the two hour section used for both the calm and windy sections, filtered and unfiltered. Only station HAG is shown, but all stations were used for the measurements.

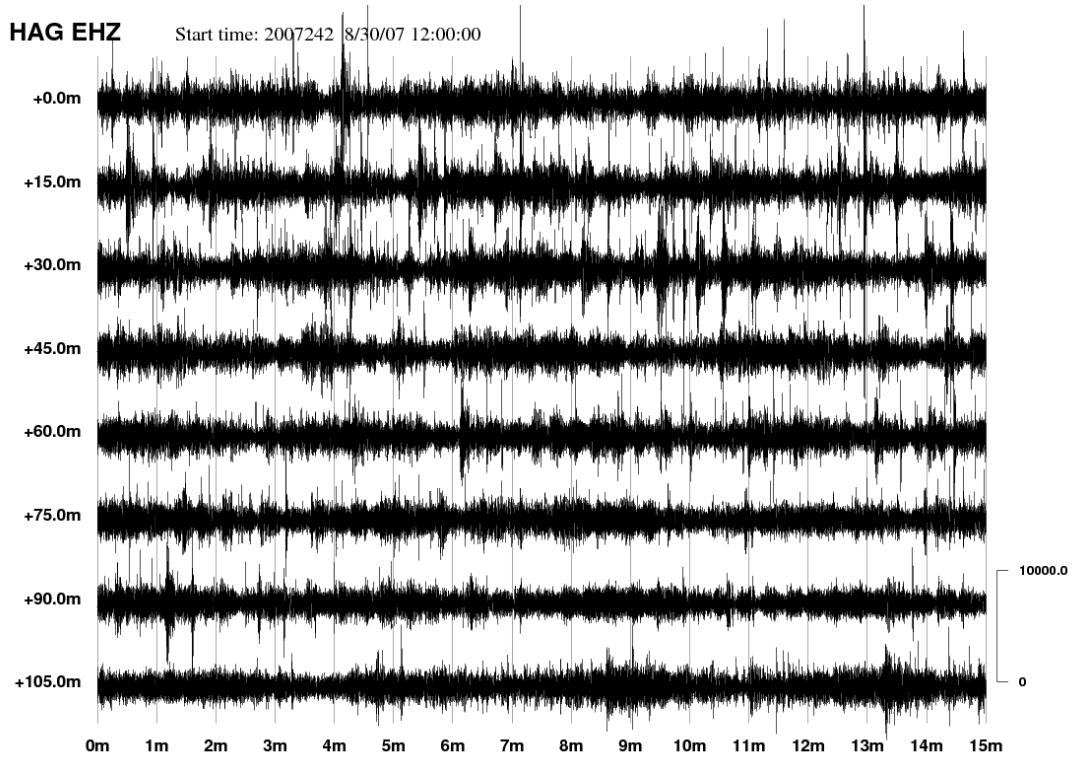

Figure E1: HAG calm, unfiltered pseudo-helicorder

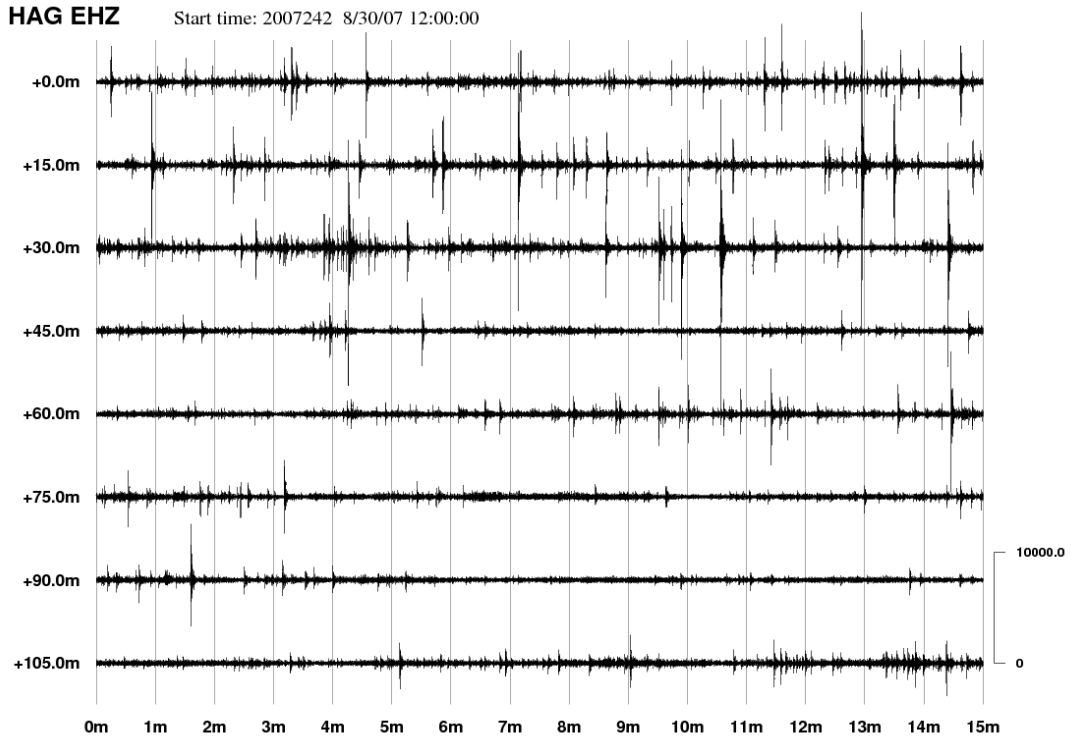

Figure E2: HAG calm, filtered pseudo-helicorder

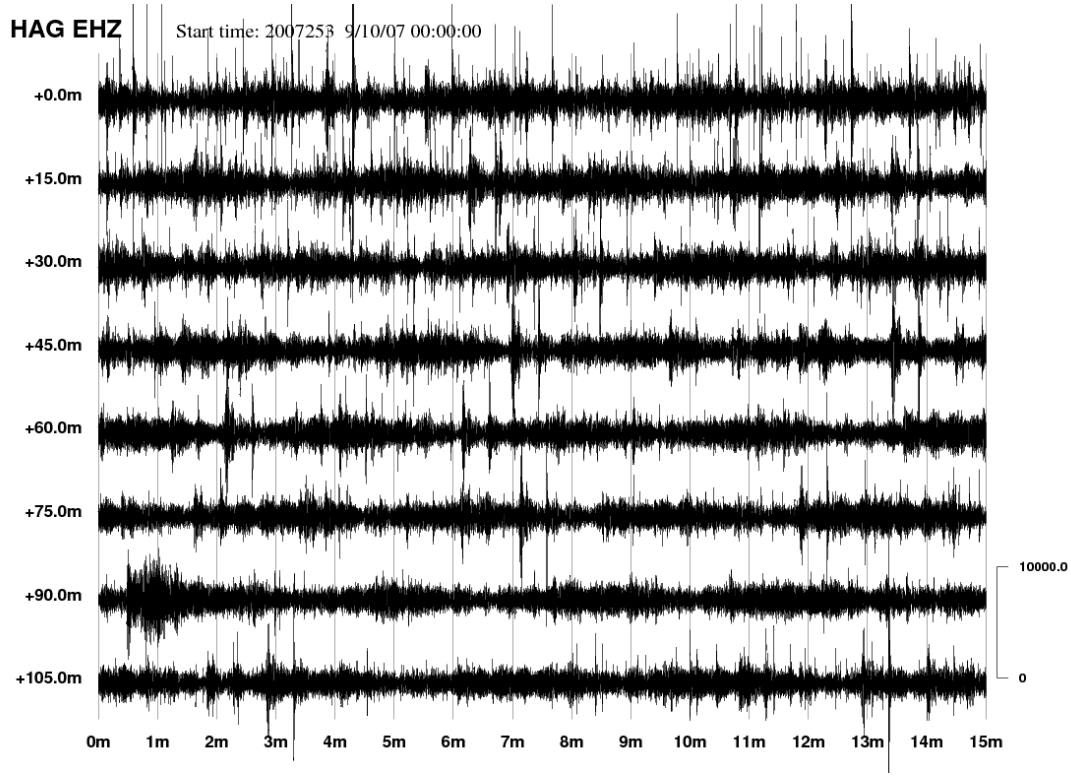

Figure E3: HAG windy, unfiltered pseudo-helicorder

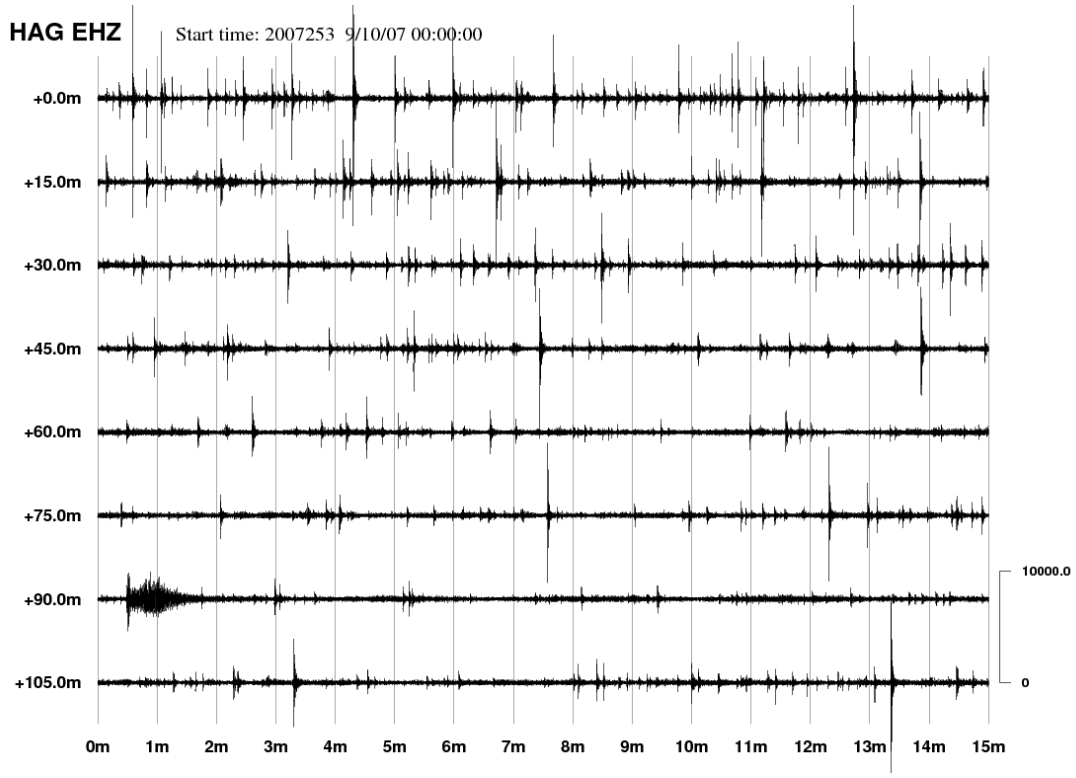

Figure E4: HAG windy, filtered pseudo-helicorder

Appendix F:

Additional Figures

Frequency Spectra

The following images are examples of the frequency spectra showing typical examples from the suite of sample waveforms for each station. The lefthand frame shows the waveform and the righthand frame shows the corresponding frequency spectrum.

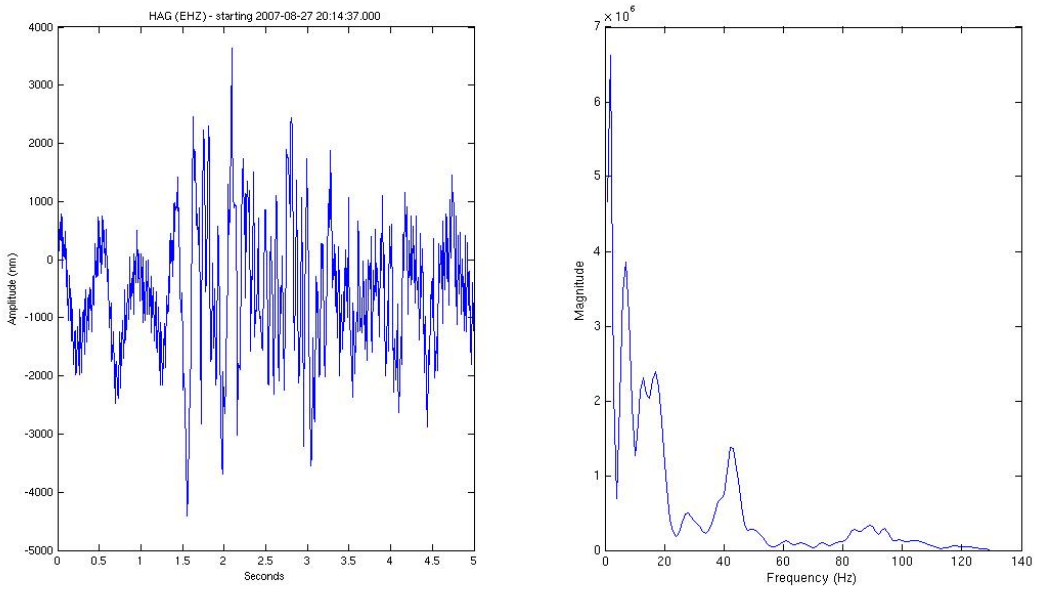

Figure F1: Station HAG frequency spectra

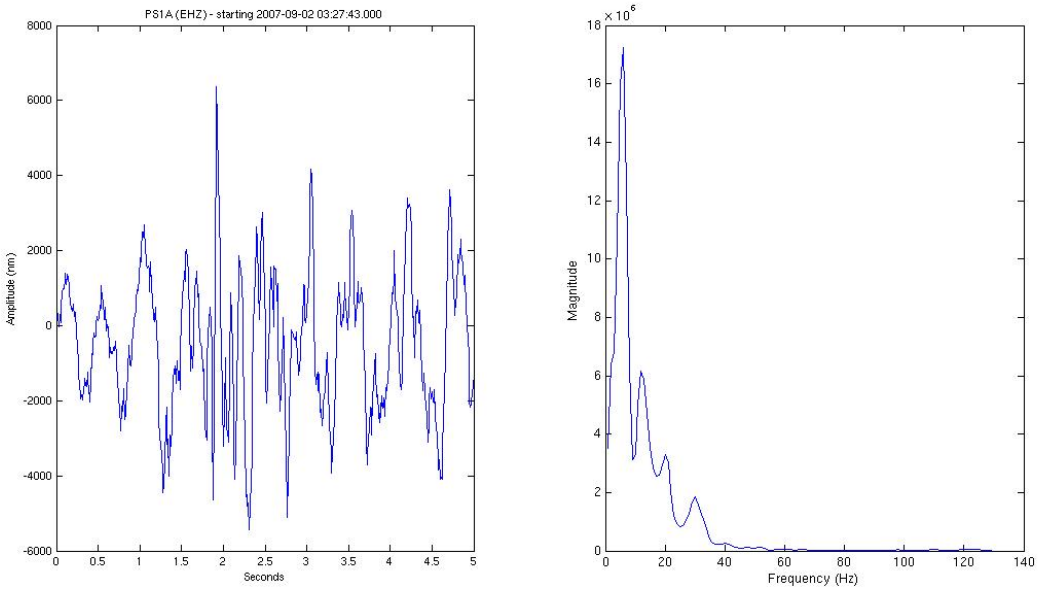

Figure F2: Station PS1A frequency spectra

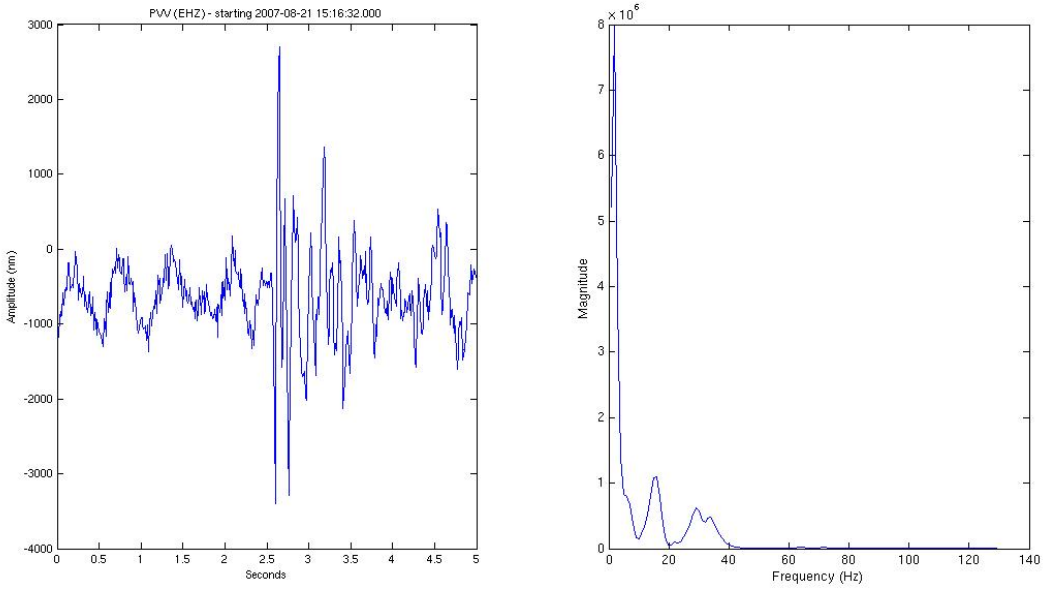

Figure F3: Station PVV frequency spectra

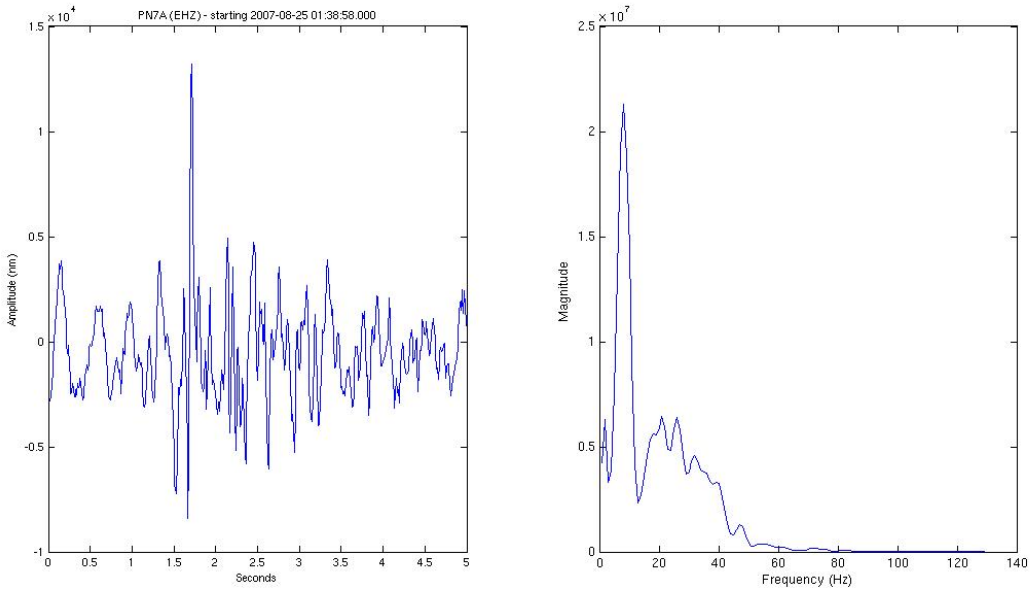

Figure F4: Station PN7A frequency spectra

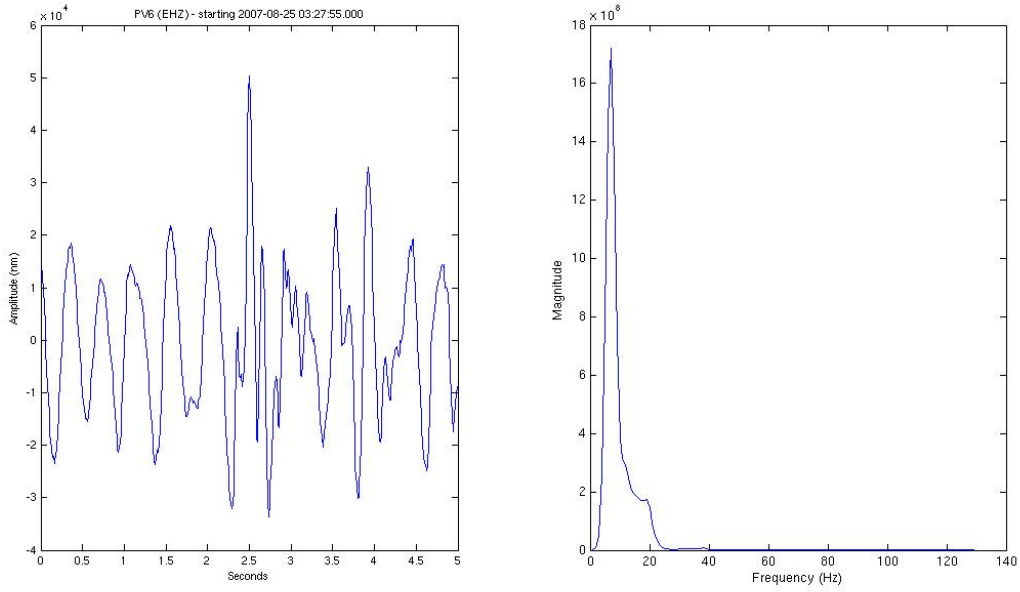

Figure F5: Station PV6 frequency spectra

Error Ranges

The following figures show the variation in the calculated values of energy and water content depending on the input variables given for frequency and temperature. For the variation of frequency temperature was kept constant at 630 degrees Celsius. For the variation of temperature the frequency was kept constant at 7 Hz.

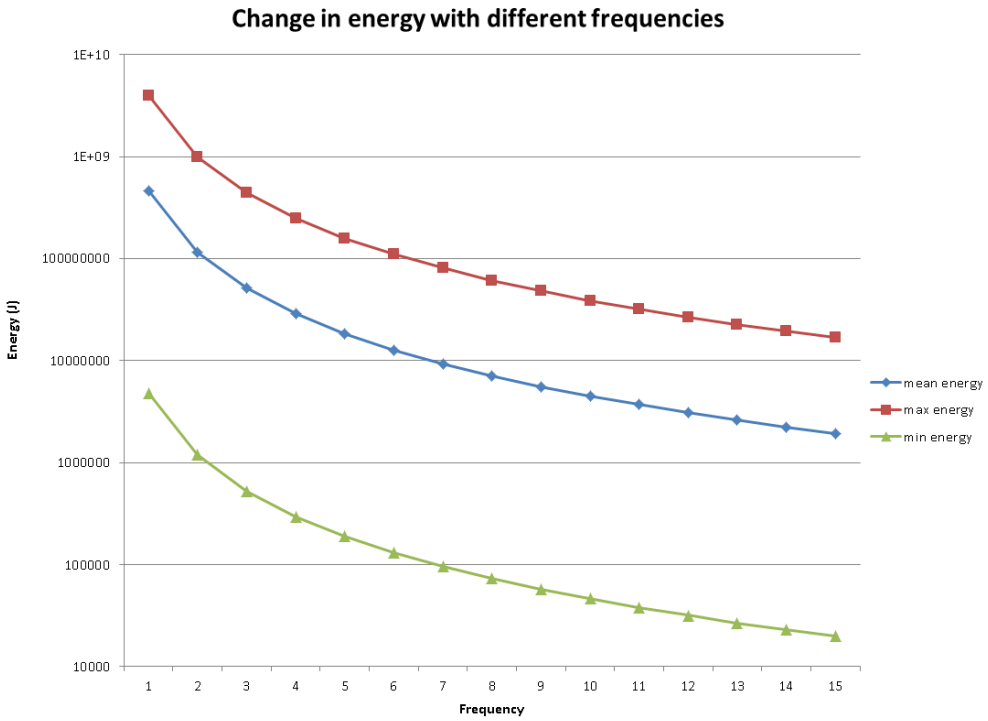

Figure F6: Change in energy with frequency

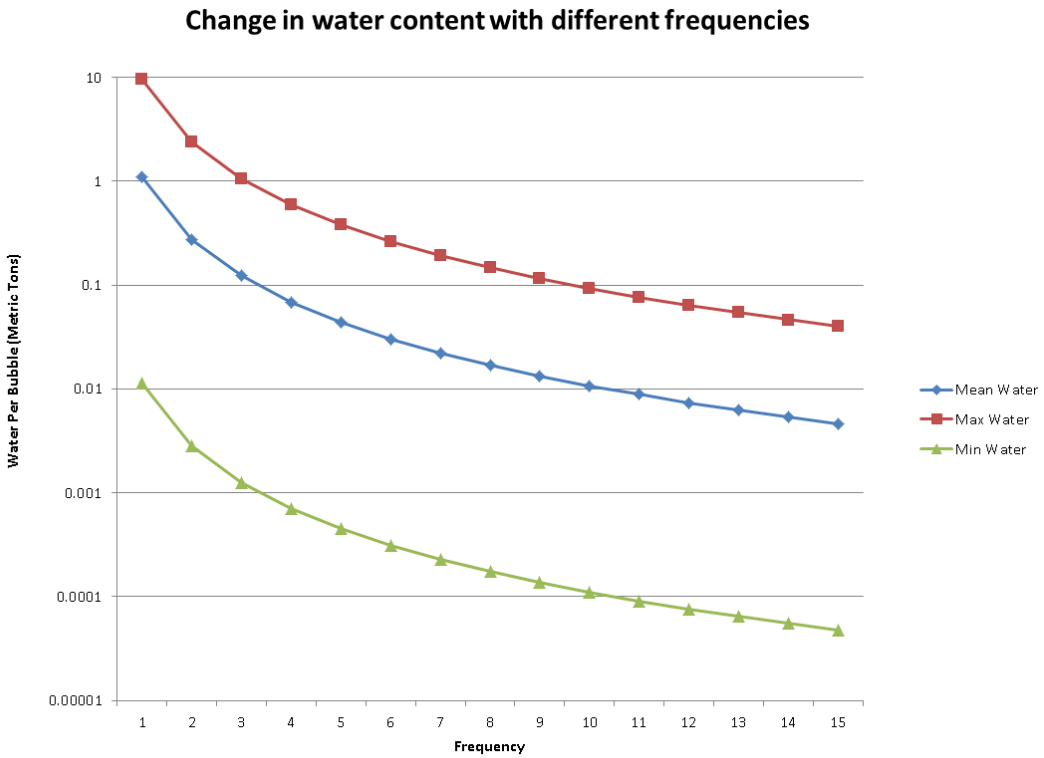

Figure F7: Change in water content with frequency

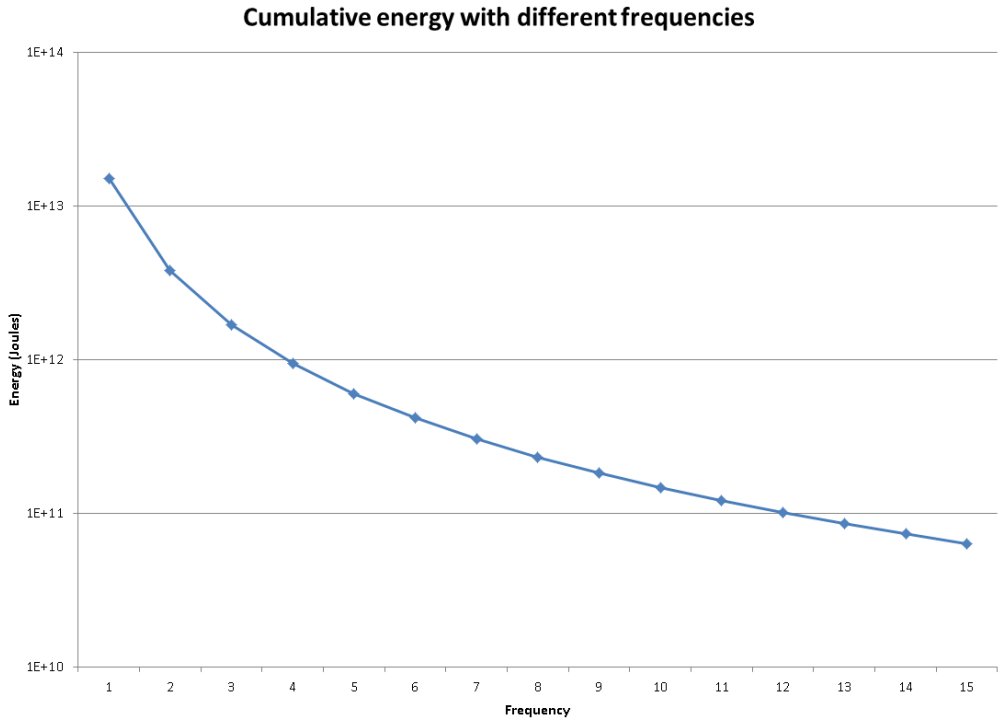

Figure F8: Change in cumulative energy with frequency

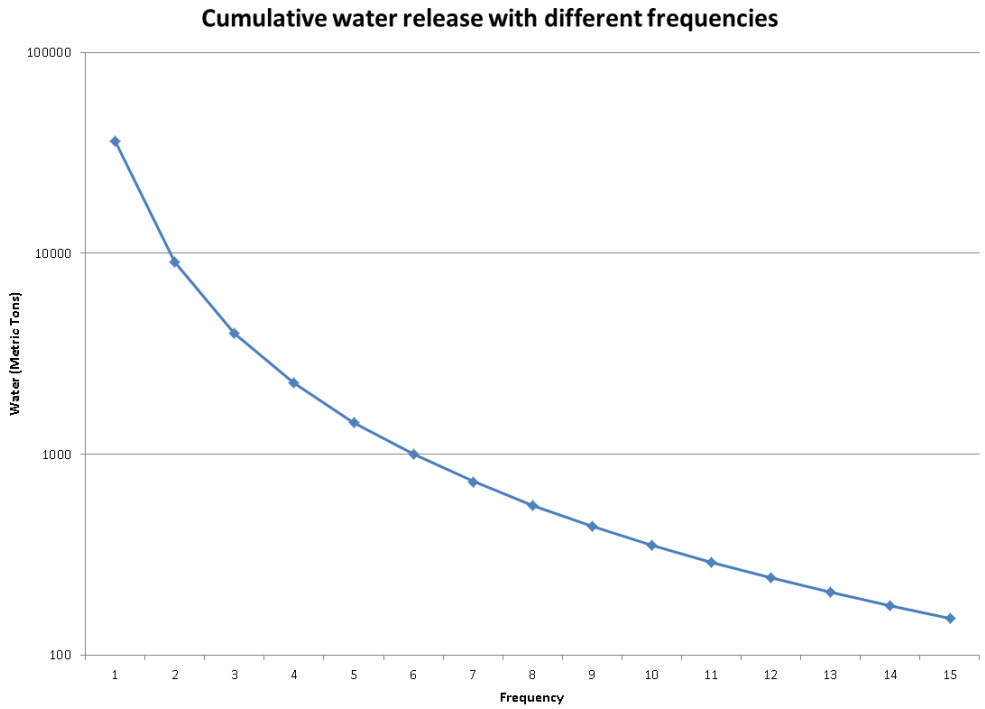

Figure F9: Change in cumulative water content with frequency

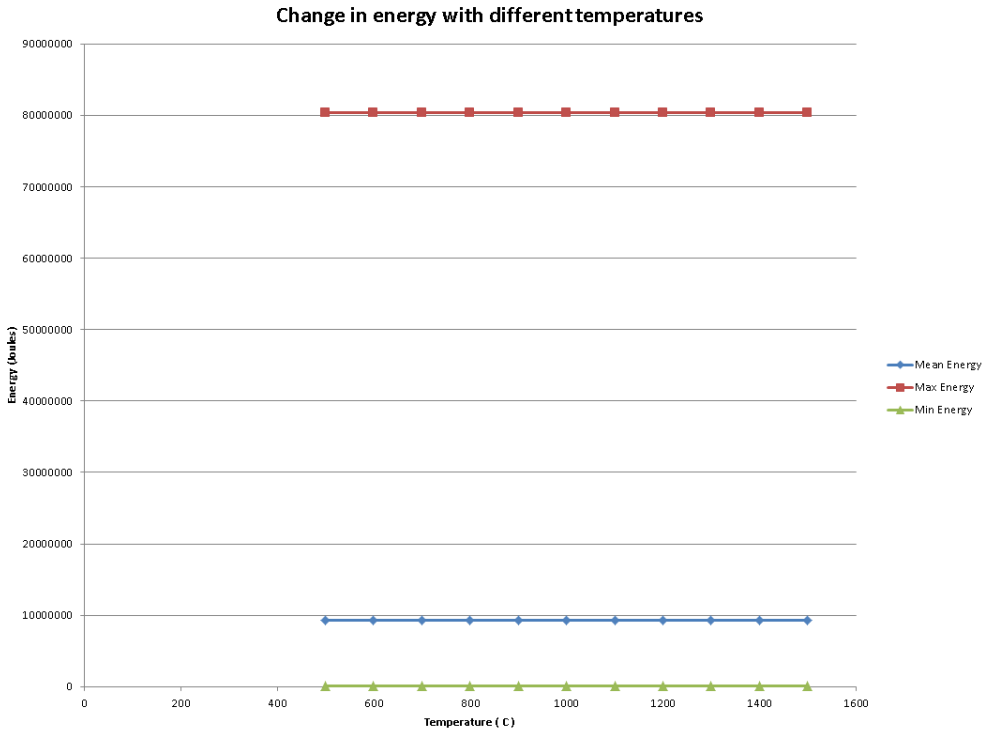

Figure F10: Change in energy with temperature

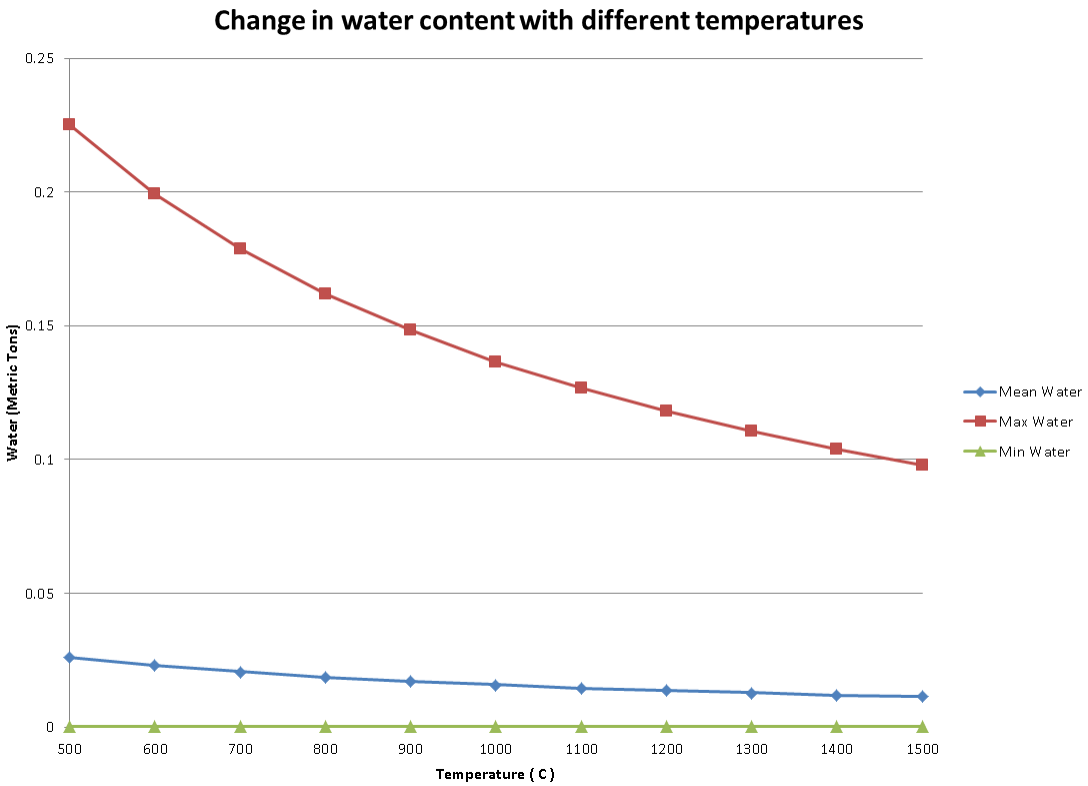

Figure F11: Change in water content with temperature

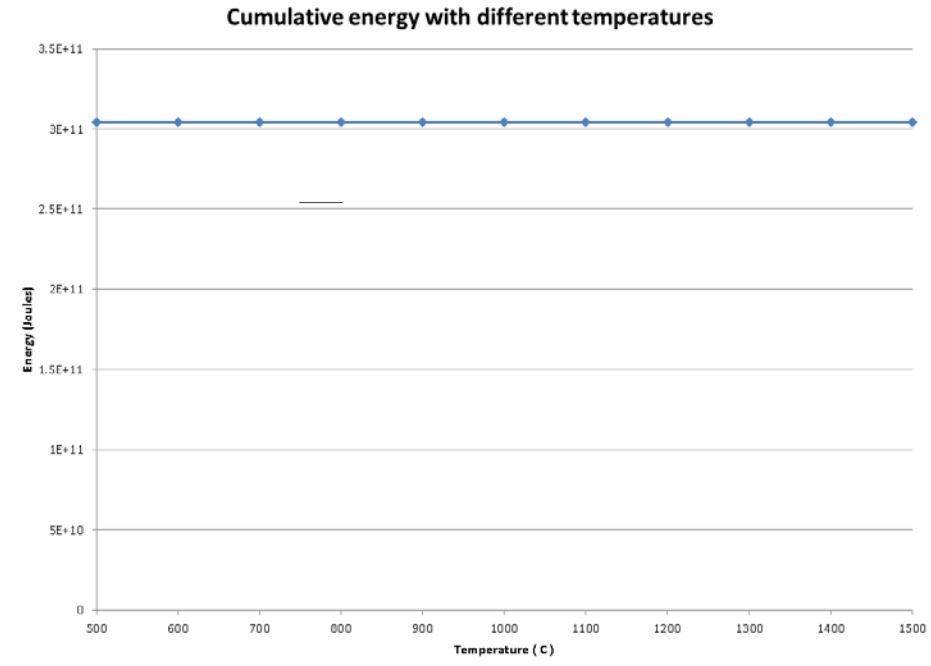

Figure F12: Change in cumulative energy with temperature

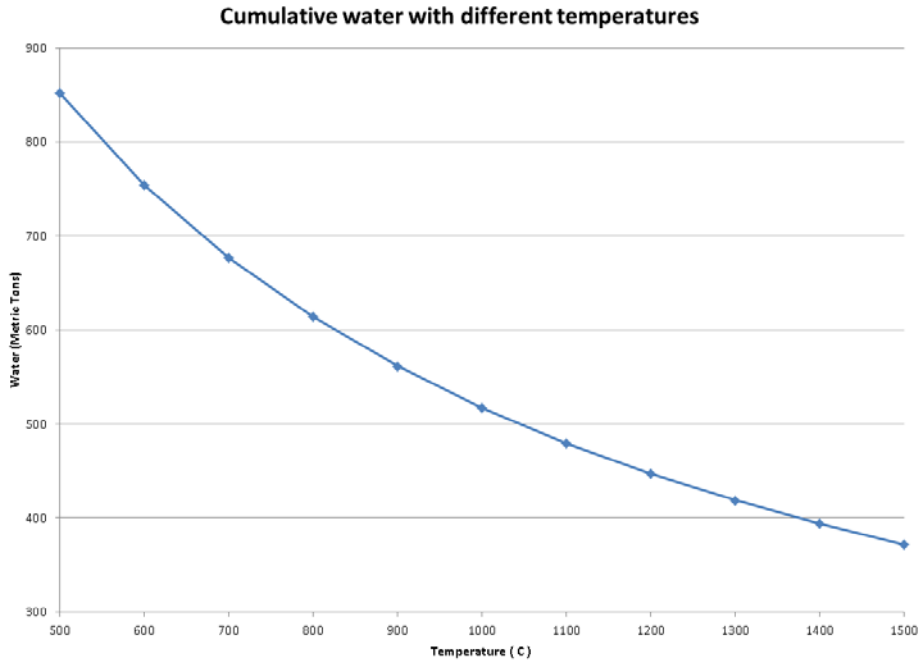

Figure F13: Change in cumulative water content with temperature